Journal of Geophysical Research: Oceans

RESEARCH ARTICLE
10.1029/2018JC013961

Structure of the Deep Spillway in the Western Part of the Romanche Fracture Zone

Roman Y. Tarakanov[1], Eugene G. Morozov[1], Hans van Haren[2], Nikolay I. Makarenko[3], and Tatiana A. Demidova[1]

[1]Shirshov Institute of Oceanology, Russian Academy of Sciences, Moscow, Russia, [2]Royal Netherlands Institute for Sea Research (NIOZ), Den Burg, Netherlands, [3]Lavrentiev Institute of Hydrodynamics, Novosibirsk, Russia

Key Points:
- The spillway in the western part of the Romanche fracture zone exists quasi-permanently in the regime of a hydraulic controlled overflow
- Transformation of the available potential energy into kinetic energy causes very intense fluctuations of velocities in the deep spillway
- We quantify transport of the abyssal flow by the deep spillway

Correspondence to:
R. Y. Tarakanov,
rtarakanov@gmail.com

Citation:
Tarakanov, R. Y., Morozov, E. G., van Haren, H., Makarenko, N. I., & Demidova, T. A. (2018). Structure of the deep spillway in the western part of the Romanche fracture zone. *Journal of Geophysical Research: Oceans*, *123*, 8508–8531. https://doi.org/10.1029/2018JC013961

Received 6 MAR 2018
Accepted 5 OCT 2018
Accepted article online 11 OCT 2018
Published online 26 NOV 2018

Abstract Structure of the deep spillway was studied on the basis of conductivity-temperature-depth, lowered acoustic Doppler current profiler, and mooring measurements in 2011–2014 in the Romanche fracture zone (22°27′–22°32′W). The spillway exists quasi-permanently in the regime of hydraulic control overflow and consists of two flows in the layer $\theta < 1.20$ °C (deeper than 4,150 m). The first flow enters the fracture from the south through a gap in the Southern Wall. The second flow is directed to the east along the narrow valley of the fracture. The sill depths of these passages are 4,570 and 4,430 m, respectively. The depths over the surrounding ridges are shallower than 4,100 m. Both flows descend to the local depression of the fracture with 5,000-m depth. Bottom potential temperatures over both sills were 0.51 °C, and the measured velocities were 20–40 cm/s. When the flows descend down the slope, they accelerate in supercritical regime. Maximal measured velocities were up to 65 cm/s. Analysis of the 189-day time series of velocities on the mooring deployed in the flow descending from the gap showed a very high level of fluctuation energy: 10 times greater than the energy of the barotropic tide at this point. The only energy source of these fluctuations is the available potential energy of the deep thermocline in the West Atlantic transforming to the kinetic energy of the deep spillway. The total transport of the bottom water below $\theta = 1.2$ °C based on the lowered acoustic Doppler current profiler measurements is estimated at 0.29–0.35 Sv, which agrees with the predicted values.

Plain Language Summary The bottom waters of the Atlantic are of the Antarctic origin. They flow from the sources in Antarctica from one deep basin to another reaching the latitudes of Europe and North America. This bottom flow passes narrow channels in the submarine ridges that separate deep basins. Long channels as the Romanche Fracture Zone (FZ) at the equator usually consist of constrictions and sills. When the bottom flow passes through such a channel, deep water spillways can be formed in the constrictions down the sills where the flow accelerates because available potential energy transforms to kinetic energy. We studied the structure and dynamics of the bottom currents in the western part of the Romanche FZ on the basis of field observations. We show that in the research site the structure of the flow has exactly this form with spillways. The temperature characteristics of the bottom flow and water transport are estimated. High intensity of kinetic energy oscillations in the spillway zone was found. The forcing can be related only to the potential energy of the bottom waters in the basin upstream the Romanche FZ. The results of this study are important for modeling ocean climate research.

1. Introduction

The equatorial Romanche and Chain fractures of the Mid-Atlantic Ridge (MAR) are the main channels for the inflow of cold abyssal waters into the subequatorial basins of the East Atlantic and the Angola Basin (Mantyla & Reid, 1983; Mercier & Speer, 1998; Morozov et al., 2010). The low temperature of these waters is due to their Antarctic origin. Very cold and dense Antarctic shelf waters descending the Antarctic slope mix with the surrounding warmer waters of circumpolar origin and reach the abyssal of the ocean (Baines & Condie, 1998; Foster & Carmack, 1976). These bottom waters then spread northward overflowing from one deep-water basin to another (Morozov et al., 2010). The overflow process generally focuses in narrow channels and fractures connecting these basins. The bottom Antarctic waters are mixed in the course of their spreading to the north with the overlying warmer deep waters of the North Atlantic origin. As a result, higher and higher temperatures are observed at the bottom along the spreading pathway of bottom waters of the Antarctic origin (Morozov et al., 2010). According to the Wüst's definition (Wüst, 1936), all the waters flowing in the Atlantic in

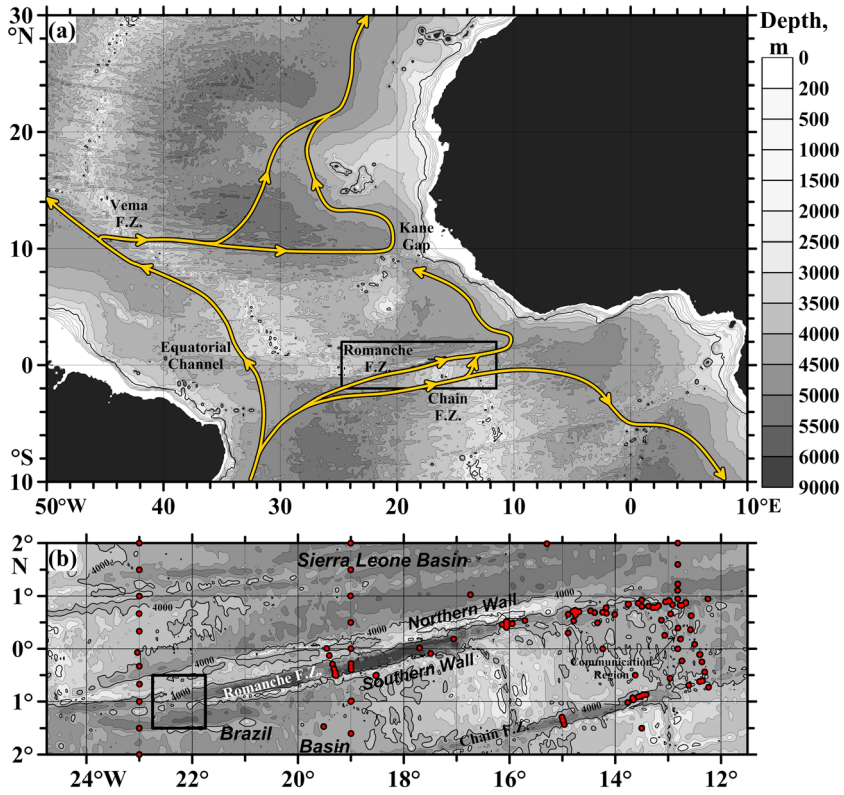

Figure 1. Scheme of AABW spreading in the equatorial and East Atlantic (a) and historical CTD stations (red circles) in the region of the Chain and Romanche fracture zones (b). Scheme shown in Figure 1a is adapted from Morozov et al. (2013). The region of the square in Figure 1b is shown larger in Figure 2. AABW = Antarctic Bottom Water; CTD = conductivity-temperature-depth.

the bottom layer from the Antarctic are called Antarctic Bottom Water (AABW). The upper limit of AABW in the equatorial zone is traditionally accepted as the isotherm (isosurface) of potential temperature θ = 1.9 °C (e.g., Mercier & Morin, 1997; Mercier & Speer, 1998). The overlying North Atlantic Deep Water (NADW) is characterized generally by a higher salinity in comparison with AABW (Wüst, 1936).

The main flow of bottom waters of the Antarctic origin in the Atlantic is concentrated in the western part of this ocean (e.g., Hogg, 2001; Morozov et al., 2010). After reaching the equatorial zone at the northern periphery of the Brazil basin, this flow divides into two branches (Figure 1a). One branch crosses the MAR through the Romanche and Chain fractures (Heezen et al., 1964; Mantyla & Reid, 1983; Mercier & Speer, 1998; Messias et al., 1999), and another branch continues its northward propagation in the West Atlantic (Hall et al., 1997; Heezen et al., 1964; Limeburner et al., 2005; Mantyla & Reid, 1983; McCartney et al., 1991; Vangriesheim, 1980; Whitehead & Worthington, 1982). The core of this flow in the Northern Hemisphere deflects to the right in accordance with the geostrophic balance; it is confined to the North Atlantic Ridge. At the same time, a partial outflow of these waters to the East Atlantic occurs through a series of fractures (Strakhov, Bogdanov, 7th N Degrees, Vernadsky, Doldrums, Arkhangelsky, 10th N Degrees, Vema, Marathon, Cabo Verde, and Kane) (Morozov et al., 2018; Tarakanov et al., 2017). The flow through the Vema fracture at 11°N is the main source of cold bottom waters in the East Atlantic basins north of this fracture up to the West European Basin (Lherminier et al., 2007; Mantyla & Reid, 1983; van Aken, 2007). The remaining part of the flow in the West Atlantic fills the abyssal of its basins in the Northern Hemisphere up to the Great Newfoundland Bank (47°N) (Mantyla & Reid, 1983; Schmitz, 1996).

The baroclinic pressure gradient between the equatorial basins of the West and East Atlantic is formed at the abyssal depths (deeper than 3,800 m near the Equator) and is directed generally to the east (Mercier & Morin, 1997). The existence of this gradient is caused by the differences in the density stratification of the abysses in these basins. A thermocline (pycnocline) exists in the abyss of the West Atlantic marking the transition from

AABW to NADW (Mercier & Morin, 1997); but the abyssal waters in the East Atlantic are generally more homogeneous and less dense. The difference in the bottom temperature (density) between these basins can reach 1.5 °C (about 0.16 kg/m^3 in density). Thus, the MAR whose crest is located at depths of 2,500–3,500 m serves as a dam that keeps colder and denser water in the West Atlantic.

The aforementioned baroclinic pressure gradient between the West and East Atlantic in the absence of the geostrophic balance in the Romanche and Chain fractures is compensated by the friction and acceleration of liquid particles (Monin, 1988). As a result, the deep thermocline in the fractures becomes eroded and the bottom temperature increases due to the interaction of the thermocline waters from the abyss of the West Atlantic with the bottom topography along the course of their eastward motion (Mercier & Morin, 1997). This process is accompanied by the release of kinetic energy from the available potential energy of the gravitational field (owing to the work of the buoyancy forces) associated with the horizontal density difference between the waters of the deep thermocline of the West Atlantic and more homogeneous abyssal waters of the East Atlantic. Such a release should be localized in the areas where the abyssal currents overflow the sills on their pathway and/or contract passing the narrows of the abyssal channels of the deep-water fractures, since acceleration of the abyssal flow can occur namely in these regions. It is clear that the dissipation of the released kinetic energy due to the bottom friction and turbulization of the flow leads to mixing of the abyssal waters. Note that overflows and flow contractions are different variants of hydraulically control process (Pratt & Whitehead, 2007).

The long Romanche and Chain fractures are series of overflows and flow contractions that are combined in a deep cataract (great waterfall; term *cataract* was introduced by Whitehead, 1989) between the West and East Atlantic. The most essential transformation of the bottom flow properties in these series due to mixing occurs where the flow spills from the main sills of the fractures (near 13°30′W in the Romanche Fracture Zone, FZ) and entrains the warmer layers overlying the deep thermocline (Mercier & Morin, 1997). Here the thermocline vanishes and the bottom temperature sharply increases (Mercier & Morin, 1997). *Strait mixing* is essential in setting the stratification of bottom waters in the World Ocean when the near-bottom current overflows a sill subjected to some kind hydraulic control process and plunges down into the downstream basin (Bryden & Nurser, 2003).

The first detailed expedition studies in the equatorial Romanche and Chain fractures were carried out in the 1990s within the French part of the World Ocean Circulation Experiment (WOCE) programs ROMANCHE-I–III (Mercier & Bryden, 1994; Mercier & Morin, 1997; Mercier & Speer, 1998). In 1991–1994, many conductivity-temperature-depth (CTD) stations were occupied and moorings were deployed in this region (Mercier et al., 1994; Mercier & Morin, 1997; Mercier & Speer, 1998). The studies were concentrated in the eastern parts of the fractures: east of 19°30′W in the Romanche and east of 15°W in the Chain FZ. Based on these projects, the pathways of the abyssal waters in the eastern parts of the fractures were studied in detail. The transport of these waters and the degree of their transformation along the propagation path were estimated in Ferron et al. (1998), Mercier et al. (1994), Mercier & Morin (1997), Mercier & Speer (1998), Messias et al. (1999), and Polzin et al. (1996). In 2005 and 2009, several stations were made by the Shirshov Institute of Oceanology of the Russian Academy of Sciences between 13°W and 16°W repeating some casts of the ROMANCHE projects. In addition to the CTD soundings at these stations, measurements of the current velocity using the lowered acoustic Doppler current profiler (LADCP) were executed. On the basis of these data, estimates of the transport of abyssal waters as well as of the temporal variability of the thermohaline properties of the flow of these waters were obtained (Demidov et al., 2006, 2012; Morozov et al., 2010). The existence of deep spillways near the sills in the eastern parts of both fractures was established (Morozov et al., 2012). In addition to the ROMANCHE projects and the Russian measurements in 2005 and 2009–2014, the FZs were intersected by transoceanic sections performed both in the framework of the WOCE/Climate and Ocean Variability, Predictability and Change projects and in the pre-WOCE period. The locations of CTD stations from the historical data array WOD13 are shown in Figure 1b giving an idea of the degree of study of the Romanche and Chain fractures.

From 2011, the Shirshov Institute of Oceanology of the Russian Academy of Sciences has been conducting field research in the western part of the Romanche FZ. In 2011, a hydrographical survey consisting of a section of five stations with CTD and LADCP casts across the fracture channel at 22°10′W, one station in the fracture channel 18 km west, and one station in the gap in the Southern Wall of the fracture at

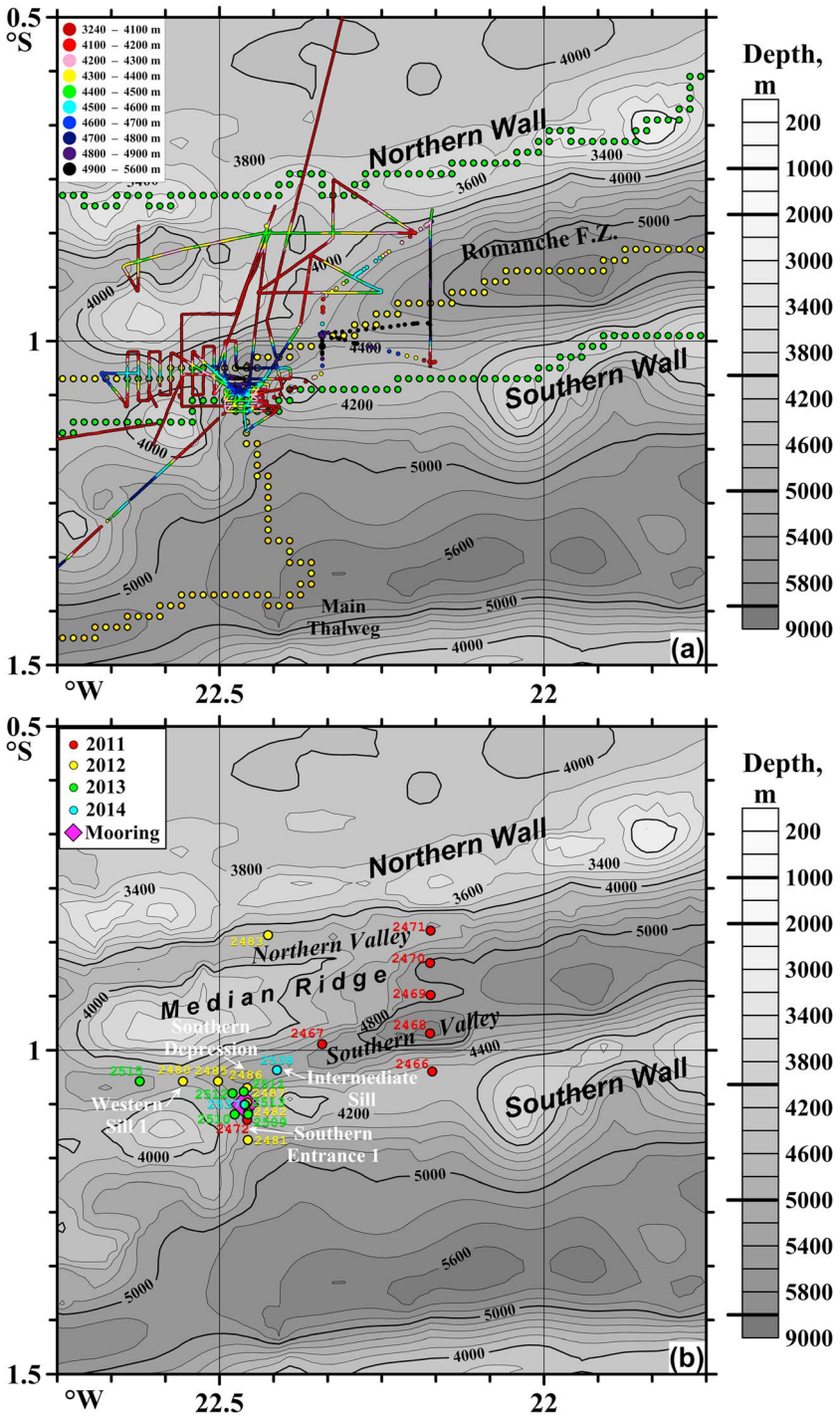

Figure 2. Bottom topography in the region of the entrance to the Romanche FZ based on the data of the recent version of database (Smith & Sandwell, 1997, V18.1; Figure 2a) and corrected using our echo soundings in 2011–2014 (Figure 2b). Color lines in Figure 2a show the lines and depths of echo-sounder measurements (see the upper left legend). Color circles and numerals in Figure 2b indicate the points and numbers of stations in 2011–2014 (see the upper left legend); FZ = fracture zone.

22°27′W was made (Figure 2b; Tarakanov et al., 2013). In addition, echo sounding of the bottom topography has been performed along the vessel's route. The configuration of the 2011 survey based of the LADCP measurements did not allow us to reveal the acceleration of the flow that enters the fracture channel through this gap. However, the existence of a deep spillway in this area was established from indirect

indications: by the erosion of the lower part of the deep thermocline with $\theta < 1.2$ °C as the current overflows the sill in this gap, and by a sharp temperature increase (from 0.51 to 0.65 °C) over a distance of only 15 miles to the east along the pathway in the fracture channel. The latter observations made it possible to estimate the coefficient of vertical turbulent exchange k_z in the area of the spillway as O(10^{-2}) m^2/s (Tarakanov et al., 2013). This value is 2 orders of magnitude greater than the canonical value (Munk & Wunsch, 1998), which is necessary to maintain the existing density stratification in the deep layer of the World Ocean, and 3 orders of magnitude greater than the values observed in the open ocean (Gregg, 1989; Polzin et al., 1996).

The field works were continued to study the structure of the spillway discovered in 2011 in the western part of the fracture. A total of 18 CTD/LADCP stations were made in 2012–2014 in this area. In addition, a mooring with two acoustic current meters and a 198-m string of 99 thermistors provided by the Royal Netherlands Institute for Sea Research was deployed from October 2013 to April 2014 at 01°05.0′S, 22°27.7′W in the flow descending from the sill of the gap in the Southern Wall of the fracture. Some preliminary estimates of the results of the field studies in 2011–2014 were published in Morozov et al. (2017) and van Haren et al. (2014).

In this paper we consider the three-dimensional structure of the deep spillway in the Romanche FZ on the basis of a set of measurement data in 2011–2014 including the half-year mooring measurements. Section 2 describes the measurement data; section 3 describes the results of measurements of the bottom relief; in sections 4 and 5 we analyze the CTD/LADCP measurements and mooring measurements, respectively; section 6 gives the estimates of the transport of bottom waters through the spillway area; and section 7 summarizes the conclusions of the paper.

2. Data and Data Processing

In 2011–2014, we occupied a total of 25 CTD/LADCP stations during four surveys in the region of the deep spillway, which we discovered in the western part of the Romanche FZ. The station layout and information about them are shown in Figure 2 and Table 1. At each station we measured temperature, electrical conductivity, and depth using the SBE-19 plus SeaCAT profiler with the SBE 33 onboard unit, and velocities using the LADCP (Teledyne RD Instruments Work Horse Sentinel, 300 kHz) mounted together with the CTD profiler on the SBE 32 frame (Carousel Water Sampler). We stopped the casts at a distance of 2–5 m above the bottom using the altimeter (model PSA-916) and pinger of the Benthos Co.

The CTD measurements were processed by the standard processing package SBE Data Processing V. 7.23.2. We used the results of precalibration and postcalibration of temperature and conductivity sensors to correct their drift. The accuracy of temperature is 0.005 °C, conductivity 0.0005 S/m, and pressure 0.1% of the 7,000 dbar full scale. Taking into account that the SBE19+ sounding frequency is 4 s^{-1}, and the characteristic speed of lowering is 0.8 m/s, the number of measurements per one level at 2-dbar averaging is 10. In this case, the accuracy of calculating temperature at one level is $0.005°/\sqrt{10} \approx 0.0015$ °C. Similarly, the accuracy of measuring practical salinity (recalculated from electrical conductivity, temperature, and pressure) is 0.0015 psu.

The data of lowered ADCP were processed using the LADCP Processing, version IX.10, whose principles are described in (Visbeck, 2002). Processing outputs the profiles of zonal and meridional velocity components with a vertical step of 8 m. Such a step approximately corresponds to the digitization of the hardware averaging of the velocity profiles measured by the LADCP and provides an estimate of the velocity recovery error at each level close to the lowest possible in the processing algorithm. This velocity error is also a result of processing the data using the specified software. In the bottom layer up to 150 m from the bottom, where the RDI BottomTrack operates, the error of the baroclinic velocity component is 1–2 cm/s, and at a greater distance from the bottom it is 7–10 cm/s. We interpreted it for the transport calculations as a continuous depth function in a discrete depth representation.

We deployed a mooring in the gap in the Southern Wall with two Aquadopp (1.5 MHz) current meters at 4,421 and 4,611 m (at 01°05.0′S, 22°27.7′W; location of the mooring is shown in Figure 2b) and 99 temperature sensors between them separated by 2 m. The mooring operated from 8 October 2013 to 16 April 2014. Details of its location are given in Table 1. The sampling interval of Aquadopp was 10 min. The accuracy of Aquadopp measurements was 1.1 and 1.6 cm/s for the horizontal and vertical components, respectively. Synchronous time sampling of the temperature sensors on the thermistor line was 1 s. Their accuracy was

Table 1
CTD/LADCP Stations and Mooring in the Western Part of the Romanche Fracture Zone

Time GMT (at the bottom)	CTD stations and mooring	Coordinates of the instrument at the bottom	Lower measurement/ocean depth (m)
		Cruise 34	
23.10.2011 01:52	2466	01°02.0′S, 22°10.3′W	4,097/4,107
23.10.2011 06:27	2467	00°59.4′S, 22°20.5′W	4,915/4,925
23.10.2011 11:12	2468	00°58.4′S, 22°10.5′W	5,571/5,581
23.10.2011 15:27	2469	00°54.9′S, 22°10.5′W	4,907/4,917
23.10.2011 19:18	2470	00°51.9′S, 22°10.5′W	5,245/5,255
23.10.2011 23:24	2471	00°48.9′S, 22°10.5′W	4,325/4,335
24.10.2011 05:25	2472	01°06.5′S, 22°27.4′W	4,613/4,623
		Cruise 36	
27.10.2012 09:57	2480	01°02.9′S, 22°33.4′W	4,430/4,437
27.10.2012 15:18	2481	01°08.3′S, 22°27.4′W	4,668/4,674
27.10.2012 19:00	2482	01°05.8′S, 22°27.3′W	4,565/4,571
28.10.2012 00:04	2483	00°49.3′S, 22°25.5′W	4,368/4,374
28.10.2012 08:30	2485	01°02.9′S, 22°30.1′W	4,728/4,735
28.10.2012 12:20	2486	01°03.5′S, 22°27.4′W	4,923/4,930
28.10.2012 16:14	2487	01°04.8′S, 22°27.4′W	4,697/4,704
		Cruise 37	
07.10.2013 10:38	2509	01°06.1′S, 22°27.5′W	4,588/4,598
07.10.2013 14:14	2510	01°06.0′S, 22°28.6′W	4,391/4,400
07.10.2013 17:55	2511	01°04.0′S, 22°28.0′W	4,987/4,997
07.10.2013 22:07	2512	01°04.0′S, 22°29.0′W	4,847/4,857
08.10.2013 12:31	2513	01°05.1′S, 22°27.7′W	4,698/4,705
08.10.2013 13:45 (time of deployment)	2514 mooring deployment	01°05.034′S,22°27.652′W	4,629
08.10.2013 16:28	2515	01°03.0′S, 22°37.5′W	4,580/4,590
09.10.2013 10:47	2516	01°15.5′S, 23°54.0′W	4,981/4,991
09.10.2013 20:00	2517	01°25.8′S, 24°00.6′W	4,899/4,908
		Cruise 38	
16.04.2014 08:20 (time of deployment)	2536 mooring recovery	01°05.227′S, 22°27.637′W	4,629
16.04.2014 17:10	2537	01°05.0′S, 22°27.7′W	4,703/4,706
16.04.2014 21:10	2538	01°01.8′S, 22°24.7′W	4,866/4,872

Note. CTD = conductivity-temperature-depth; LADCP = lowered acoustic Doppler current profiler.

0.0005 °C (van Haren et al., 2014). In this paper, we used the data from only two thermistors to analyze the long-term changes at the mooring point: the lowest thermistor was located 9 m over the bottom (4,609 m), and the uppermost at a depth of 4,425 m. To recalculate the in situ temperature of these sensors into the potential temperature, the linear regression coefficients between the temperature and salinity in the AABW layer were determined from the *yo-yo* measurements executed at stations 2513 and 2537 in the layer from bottom to a depth of 300 m above the bottom. The basis for this approximation is the quasi-linear relationship between the potential temperature and salinity in the AABW layer in the Romanche FZ (Figure 3); a deviation from this dependence arises only in the NADW layer in the form of bending in the core layer of this water. The calculated salinity was then used to calculate the potential temperature. The accuracy of this procedure (~0.0001 °C) is better than the measuring accuracy of the thermistor. We also note that the quasi-linear relationship between temperature and salinity means that salinity does not provide additional information on the structure of the spillway. Therefore, we do not show more salinity curves in this paper.

The barotropic tidal velocities in the region were calculated from the TOPEX/Poseidon satellite data using the National Aeronautics and Space Administration 0.25° × 0.25° database (TPXO 7.2 model) available at the Oregon State University (Egbert & Erofeeva, 2002). In addition, the total tidal velocities were estimated from the mooring measurements. Based on the results of the comparison of these methods of estimating tidal velocities, we subtracted the barotropic tidal velocities from the measurements of LADCP data.

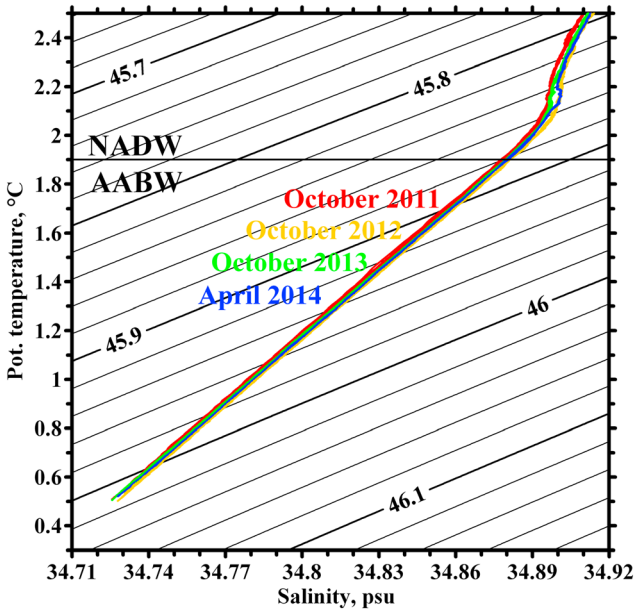

Figure 3. A θ,S diagram for the abyssal layers in the Romanche FZ. The red color indicates the stations in 2011, yellow in 2012, green in 2013, and blue in 2014. Solid black lines indicate density anomaly referenced to 4,000 dbar. The horizontal line along θ = 1.9 °C shows the boundary between NADW and AABW. NADW = North Atlantic Deep Water; AABW = Antarctic Bottom Water; FZ = fracture zone.

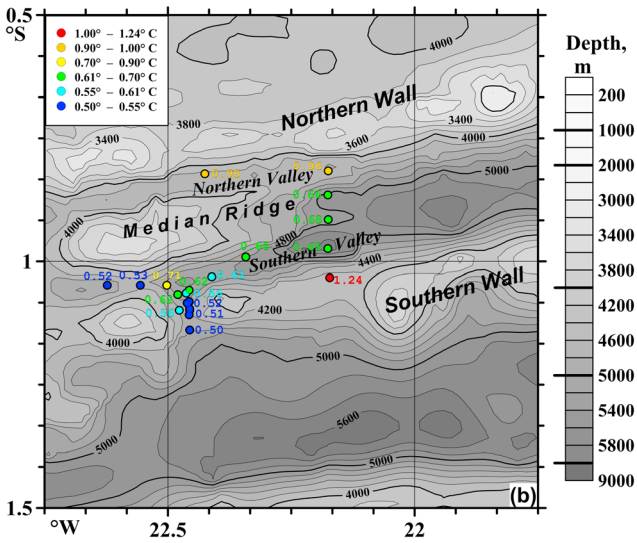

Figure 4. Potential temperatures at the lowest CTD points (~5–10 m) above the ocean bottom based on the CTD measurements at stations in 2011–2014. CTD = conductivity-temperature-depth.

We used the bottom topography from the 1-min digital array (Smith & Sandwell, 1997) V.18.1. However, our measurements in 2011 in the region showed that the difference between the digital bottom array and the actual depths can be as high as 700 m (Tarakanov et al., 2013). Therefore, we carried out a detailed survey of the region with parallel tracks separated by 1–2 miles using the ELAC LAZ 4700 echo sounder. Since the echo sounder is tuned to a sound velocity of 1,500 m/s in the entire water column, the results of these measurements were corrected taking into account the actual sound velocity estimated from the CTD measurements. Figure 2a shows the bottom relief based on (Smith & Sandwell, 1997) along with the trajectory of the vessel, and Figure 2b shows the bottom relief, corrected according to our echo-sounder measurements, that we used when plotting the figures of sections.

3. Bottom Topography in the Deep Spillway Region

Knowledge of the bottom topography is necessary to describe the structure of the spillway in the western part of the Romanche FZ. The fracture is a channel oriented practically from west to east between the Southern and Northern walls (ridges, Figure 1b). The characteristic depths above the crests of the Southern Wall around the spillway are 3,500–4,100 m, and those of the Northern Wall are 3,200–3,600 m. The Median Ridge extends along the channel (approximately, in the middle of its cross section) and divides the channel into the Southern and Northern Valleys (channels, Figure 2). The crest of this ridge rises to a depth of 3,400–4,000 m approximately at 22°20′–22°40′W and rapidly descends to the east to almost 5,000 m already at 22°10′W. The Northern Valley of the fracture at the segment adjacent to the minimum depths above the Median Ridge has almost flat bottom at its deepest part based on the echo-sounder measurements along the tracks transverse and parallel to the valley. The width of the valley at a level of the 4,150-m isobath is 5–10 km (Figure 2b); the choice of this particular isobath for characterizing the width is related to the dynamic structure of the spillway in the western part of the Romanche fracture. This isobath approximately corresponds to an isotherm of θ = 1.2 °C, which is approximately the upper boundary of the spillway layer (Tarakanov et al., 2013). It is likely that the sill depth of the Northern Valley in this segment does not exceed 4,300 m. In the eastern direction the valley depth becomes deeper than 5,200 m already at 22°10′W. The Southern Valley at 22°33.5′W has a sill with a depth of about 4,430 m (Western Sill-1 according to Tarakanov et al., 2013) (Figure 2). This sill also coincides with the extreme narrowness of the valley. Here its width at the 4,150-m isobath is about 2 km. Further to the east, the valley widens significantly and deepens, reaching 5,000 m in the local deepening at 22°28′W (hereinafter, the Southern Depression). Even farther to the east, the Southern Valley becomes shallower (4,870 m) and narrows to 5.5 km at 22°24.5′W (hereinafter, the Intermediate Sill) and again deepens to 5,600 m at 22°10′W. A gap (passage) with a sill depth of about 4,560 m exists in the Southern Wall of the fracture at the longitude of the Southern Depression (Southern Entrance-1 according to Tarakanov et al., 2013). The width of this passage, which connects the Romanche FZ with the fracture to the south, is about 7.5 km at a depth of the 4,150-m isobath.

4. CTD/LADCP Observations in the Deep Spillway Region

4.1. Temperature

As we mentioned in section 1, the indirect attributes, which allowed us to reveal in 2011 the presence of a spillway in the western part of the Romanche fracture, were the erosion of the lower part of the deep

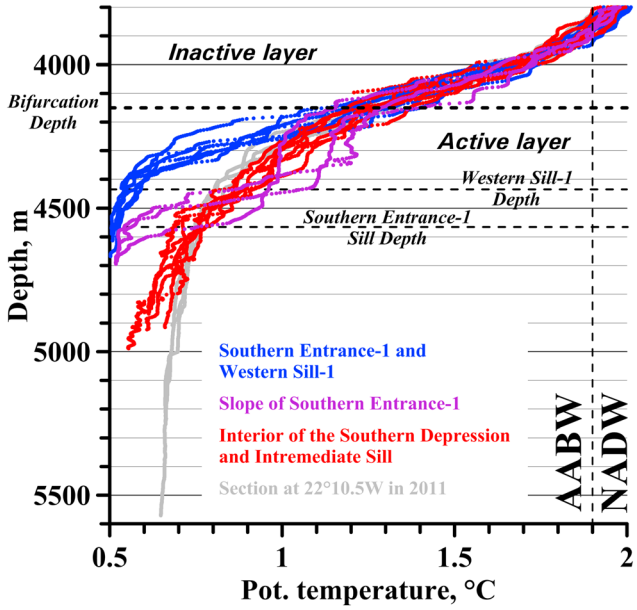

Figure 5. Potential temperature curves at stations near Southern Entrance-1 and Western Sill-1 (blue), at the slope of Southern Entrance-1 (magenta), in the interior of the Southern Depression and Intermediate Sill (red), and section at 22°10′W in 2011. The bifurcation depth splitting temperature profiles between the sills and the interior of the Southern Depression is shown. This level corresponds a boundary between inactive (motionless) and active layer in 1.5 layer model of the hydraulically controlled flow through the channel with a rectangular section between two basins (Whitehead et al., 1974). The sill depths of Southern Entrance-1 and Western Sill-1 are shown. NADW = North Atlantic Deep Water; AABW = Antarctic Bottom Water.

thermocline and the increase in temperature at the bottom over a very short distance along the abyssal flow (Tarakanov et al., 2013). To illustrate these effects, Figure 4 shows the distribution of the potential temperature measured at the CTD stations near the bottom in the region of the deep spillway, Figure 5 shows the potential temperature distributions at all stations 2011–2014, and Figures 6a, 7a, 8a, 9a show the same for 2011, 2012, 2013, and 2014, separately. We note that these measurements significantly supplemented the results of our field studies in 2011.

1. Figure 5 shows that all profiles in Western Sill-1 and Southern Entrance-1 in all years of observation form one group similar in shape, the profiles within the Southern Depression and further to the east along the fracture form the other, and the profiles above the fault slope opposite to Southern Entrance-1 form the third. Thus, the spatial variability of the temperature field between these regions during the measurement periods is much greater than the temporal (intersurvey) variability of this field. Groups of profiles are merged together at a distance from the bottom and diverge at a level of about 4,150 m, which corresponds to a temperature of $\theta = 1.2$ °C. Following Whitehead (1998) we will call this level a bifurcation depth.
2. The above erosion of the lower part of the deep thermocline (below $\theta = 1.2$ °C) between the sills and the interior of the Southern Depression indicates the presence of a hydrostatic pressure difference directed into the Southern Depression increasing with depth (as a sequence of the hydrostatic equation) with nearly the same values in different years. This pressure difference sets the abyssal flow in motion with almost the same (both qualitatively and quantitatively) dynamics of currents in each survey measurements.
3. Southern Entrance-1 is not the only source of cold abyssal waters with $\theta < 1.2$ °C for the eastern part of the Romanche FZ, as we assumed in Tarakanov et al. (2013), since an additional part of this abyssal water comes from the western part of the fracture through Western Sill-1. The potential temperature near the bottom at Western Sill-1 in the Southern Valley of the fracture was 0.534 °C in 2012 and 0.524 °C in 2013 at the point slightly displaced to the west (Figure 4). These values are close to those measured at the sill of Southern Entrance-1 (0.513 °C in 2012 and 0.506 °C in 2013, Figures 4, 7, and 8). Thus, the investigated deep spillway is formed from two flows of water of almost the same temperature range ($\theta < 1.2$ °C) that merge after descending from these sills into the Southern Depression.
4. The values of temperature near the bottom generally increase from the sills into the Southern Depression, where the temperature increase is the highest over the study site, and then to the east through the Intermediate Sill to the deep part of the Romanche FZ. This increase is from 0.506 to 0.534 °C at the upstream sills to 0.612 °C at the Intermediate Sill, and to 0.648 °C in the deep part. It is consistent with the condition for the conservation of heat with mixing inside the abyssal flow; high intensity of mixing in this region is shown in Tarakanov et al. (2013) and van Haren et al. (2014). The presence of a local temperature maximum in the eastern part of the Southern Depression (yellow bullet in Figure 4) is due to the fact that the corresponding CTD cast at the station, located on the slope of the depression at Western Sill-1, did not hit the coldest flow descending from this sill. The local maximum immediately after the Intermediate Sill ($\theta = 0.66$ °C, green bullet in Figure 4) is a consequence of the position of the station on the northern slope of the Southern Valley. Thus, despite the fact that temperature measurements shown in Figure 4 were performed in different years, we can argue that temporal variability of temperature of the abyssal flow did not distort the distribution of near-bottom temperature intrinsic for the mixing process, even near the upstream sills and in the downstream interior of the Romanche FZ, where local spatial variability has a smaller scale than the one between these regions.
5. The bottom potential temperature in the Northern Valley of the Romanche FZ in 2012 at station 2483 was 0.949 °C (Figure 4). In this case, the deep thermocline in the layer with $\theta < 1.2$ °C is already eroded as can

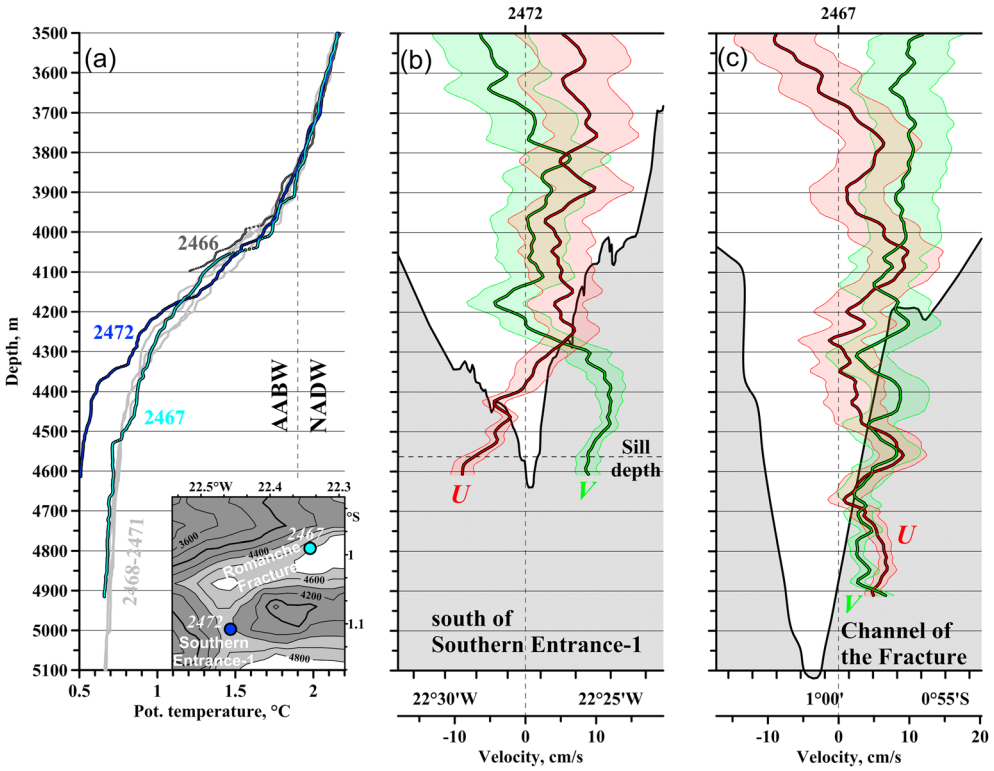

Figure 6. Profiles of potential temperature in the deep part of the study region in 2011 (a), zonal (*U*) and meridional (*V*) velocity components and errors based on LADCP measurements at station 2472 south of Southern Entrance-1 (b), and at solitary station 2467 in the southern canyon of the fracture (c). The bottom topography shown in Figures 6b and 6c in the section of Southern Entrance-1 and channel of the fracture is based on the data of echo soundings in 2011. A scheme of locations of stations 2467 and 2472 in the fracture is shown in the inset of Figure 6a. Figure 6 was adapted from Tarakanov et al. (2013). NADW = North Atlantic Deep Water; AABW = Antarctic Bottom Water.

be seen in the vertical profile (see Figure 7), that is, this station is located downstream the region where this erosion takes place. As we did not find a local depression that can be a hydraulic jump's bath in the Northern Valley where this erosion could have been, the part of the valley where we occupied the station is most likely filled through the Southern Depression rather than from the west along the valley.

4.2. Structure of the Bottom Current

To illustrate the structure of currents in the region of the spillway in the western part of the Romanche FZ, Figure 10 shows the velocity vectors in the bottom layer based on the LADCP measurements in all years of observations, Figures 6–9 show velocity profiles (along with the accuracy range) in the depth layer at stations near the sills in 2011–2014, and Figure 11 shows the sections executed in 2012 across the sill of Southern Entrance-1 and in 2013 along the flow descending from this sill. The direction of currents in the bottom layer in Figure 10 corresponds to the direction of the temperature (and pressure) gradient from the sills into the Southern Depression as described in the previous section: the abyssal flows pass through Southern Entrance-1 and Western Sill-1 to the north and to the east, respectively, and descend into the Southern Depression; then they merge into the flow that rises eastward to the Intermediate Sill and continues to move further east along the fracture channel. The measured velocities of the abyssal flow were 5–10 cm/s in front of Southern Entrance-1 and Western Sill-1, 20–25 cm/s at Southern Entrance-1, and 35 cm/s at Western Sill-1 (Figures 6–8 and 10). The maximum velocity (up to 48 cm/s) was measured on the slope of the Romanche FZ at Southern Entrance-1. Lower velocities up to 28 cm/s were fixed at the Intermediate Sill (Figure 10).

Such a velocity field as in Figure 10 is intrinsic of a hydraulically controlled overflow when the flow is accelerated in the subcritical regime (Froude number $Fr < 1$) before the control point (sill or narrows), reaches critical regime ($Fr = 1$) at this point, and transfers in the supercritical ($Fr > 1$) after its passage with a return to the subcritical regime downstream in the form of a hydraulic jump. The Froude number is defined as $Fr = u/$

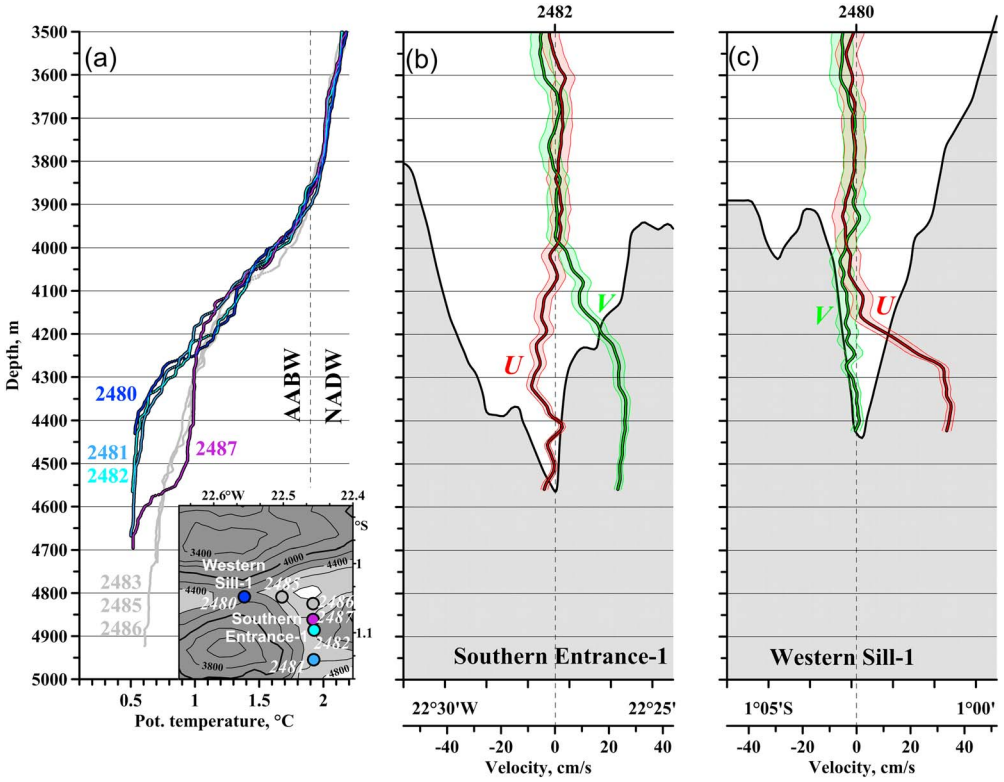

Figure 7. Profiles of potential temperature in the deep part of the study region in 2012 (a), zonal (*U*) and meridional (*V*) velocity components and errors based on LADCP measurements at station 2482 in Southern Entrance-1 (b), and at station 2480 at Western Sill-1 in the southern canyon of the fracture (c). The bottom topography shown in Figures 7b and 7c in the section of Southern Entrance-1 and Western Sill-1 is based on the data of echo soundings in 2012. The inset in Figure 7a shows a scheme of the location of stations in 2012 excluding station 2483. NADW = North Atlantic Deep Water; AABW = Antarctic Bottom Water.

$\sqrt{g'H}$; here u is the flow velocity, $\sqrt{g'H}$ is gravity wave speed in shallow water in the flow with thickness H; $g' = g\Delta\rho/\rho$ is reduced gravity acceleration; ρ is in situ density; and small value $\Delta\rho$ is the difference between the density of the flow and surrounding water. The existing data set allows us to specify a few more indirect evidences of hydraulically controlled overflow across the sills of Western Sill-1 and Southern Entrance-1.

1. We calculated the so-called predicted transport through these sills using an inviscid 1½-layer model of hydraulically controlled overflow between two basins through a channel with a rectangular cross section (Whitehead et al., 1974). In this steady model, flow Q is derived from the Bernoulli's law for the lower active layer (see Figure 5), for which potential vorticity conservation and geostrophic balance are applied. Considering that the Romance FZ is in the equatorial zone, transport Q depends only on the width W and the upstream thickness of the active layer h_u above the channel bottom, and also on the reduced gravity g':

$$Q = \left(\frac{2}{3}\right)^{\frac{3}{2}} W h_u \sqrt{g' h_u} \tag{1}$$

In accordance with Whitehead (1998) g' is estimated from upstream-downstream density difference $\Delta\rho$. In our case, we do not have enough distant upstream stations from the sill. Therefore, we used the value of the difference between the sills and the Southern Depression interior averaged over all measurements (Figure 5), which amounted to $\Delta\rho$ = 0.027 kg/m^3 (at a depth of 4,400 m). The corresponding value is $g' = 2.7 \times 10^{-4}$ m/s^2. Thickness h_u is estimated as the depth difference between the bifurcation depth and the channel bottom at the sill. This value is 280 m for Western Sill-1, and 410 m for Southern Entrance-1. Since the actual cross-sectional area of the passages is much smaller than the rectangular model cross section, we used the values W averaged over depths (below bifurcation depth), which

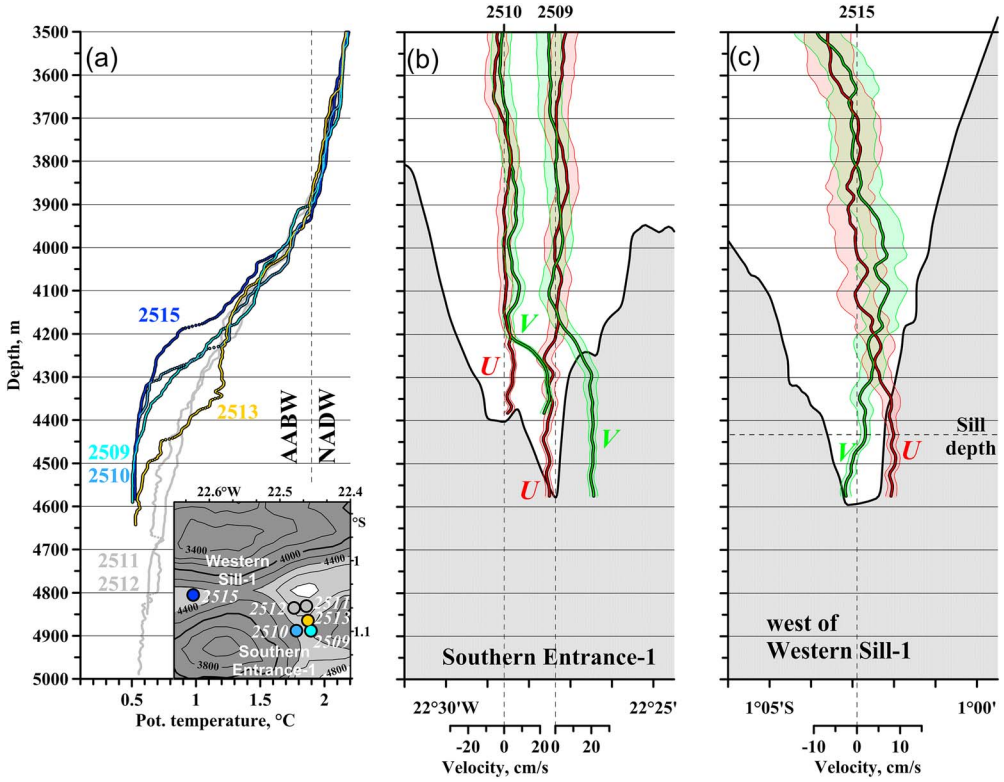

Figure 8. Profiles of potential temperature in the deep part of the study region in 2013 (a), profiles of the zonal (*U*) and meridional (*V*) velocity components and errors based on LADCP measurements across Southern Entrance-1 (b), and zonal (*U*) and meridional (*V*) velocity components at station 2515 west of Western Sill-1 in the southern canyon of the fracture (c). The bottom topography shown in Figures 8b and 8c in the section of Southern Entrance-1 and Western Sill-1 is based on the data of echo soundings in 2013. The inset in Figure 8a shows a scheme of the location of stations in 2013. NADW = North Atlantic Deep Water; AABW = Antarctic Bottom Water.

were 1.4 km and 3.2 km, respectively. Using these parameters we have 0.06 Sv for Western Sill-1 and 0.24 Sv for Southern Entrance-1. These estimates are consistent with the transport estimates based on the direct measurements (see section 6).

2. Using the same 1½-layer model, we estimated the horizontal gravity wave speed $\sqrt{g'H}$. In order to take into account the difference of the real cross section on the sills from the rectangular model, we used not the h_u, but the average thickness of the layer below bifurcation depth, which was 160 m for Western Sill-1 and 185 m for Southern Entrance-1. With these parameters the gravity wave speeds were 21 and 22 cm/s, respectively. These values are close to the measured velocities for Southern Entrance-1 (20–25 cm/s) but are significantly smaller than for Western Sill-1 (35 cm/s). This ratio of the gravity wave speed and the measured velocity at Western Sill-1 corresponds already to the supercritical flow.
3. Another feature of hydraulically controlled overflow across the sill is an uplift of the deep upstream water, which is termed *Bernoulli aspiration* (Kinder & Bryden, 1990). This is manifested, in particular, in the inclination of isopycnal (isotherm) quasi-parallel to the bottom slope and also in the acceleration of this deep upstream water. This situation was observed in the section in 2012 carried out across the sill of Southern Entrance-1 (Figure 11a), where the upward isotherm slope from the station in front of the sill was observed in the layer approximately $\theta < 0.75$ °C. The flow velocities directed toward the sills in the layer below the sill depth are fixed at two more stations located upstream relative to these sills. These are stations 2472 south of the sill of Southern Entrance-1 (Figure 6) and 2515 west of Western Sill-1 (Figure 8). Following Clément et al. (2017) we estimated the thickness of the layer below the sills as the value of the order of magnitude that can be involved in the uplifting. This is u/N, where u is the velocity at the sill, and N is the Brunt-Väisälä frequency intrinsic for the upstream basin. Given $N = 0.7 \times 10^{-3}$ s^{-1} (near the bottom layer at station 2481 just south of Southern Entrance-1), $u = 25$ cm/s at Southern Entrance-1, and

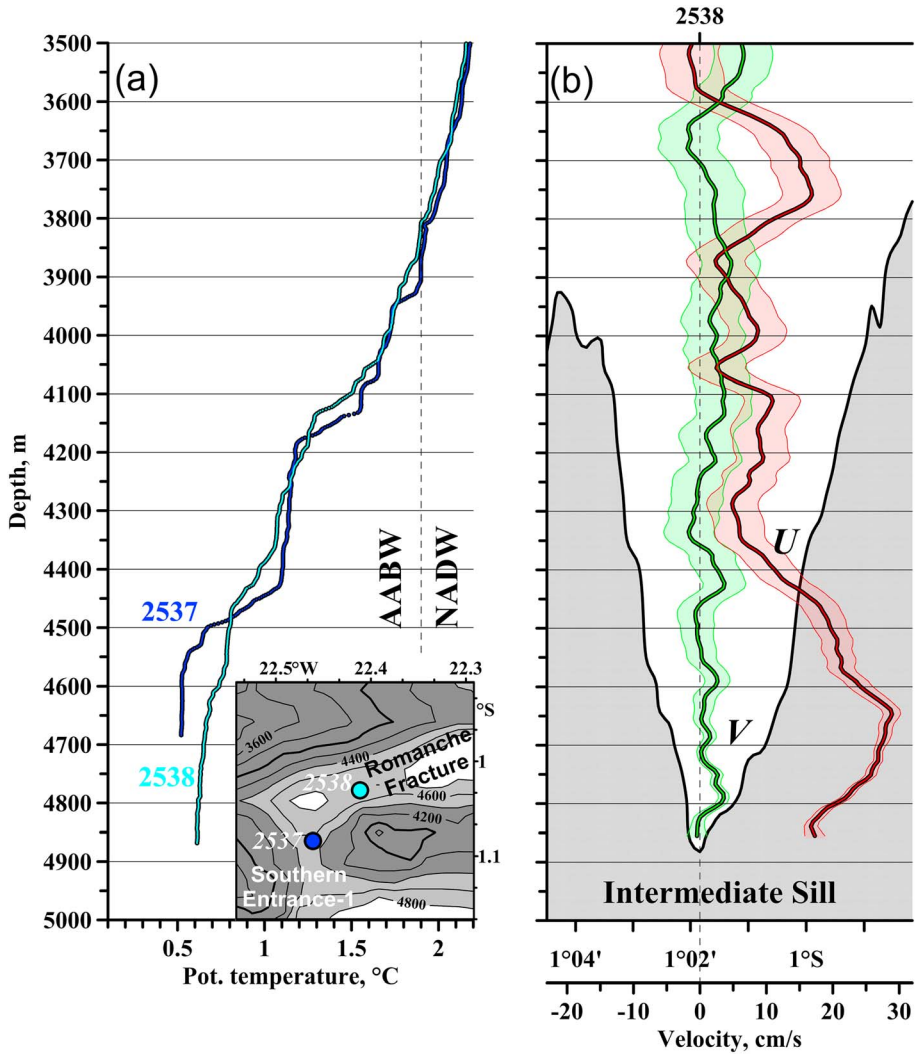

Figure 9. Profiles of potential temperature in the deep part of the study region in 2014 (a), zonal (*U*) and meridional (*V*) velocity components based on LADCP measurements at station 2538 in the southern canyon of the fracture (b). The bottom topography shown in Figure 9b is based on the data of echo soundings in 2014. The inset in Figure 9a shows a scheme of the location of stations in 2014. NADW = North Atlantic Deep Water; AABW = Antarctic Bottom Water.

35 cm/s at Western Sill-1, we get the estimates of 350 and 500 m, respectively. These estimates indicate that the bottom layers of the fracture south of the Romanche FZ, for which the depths of 5,200–5,700 m are characteristic, can be blocked from the inflow into the Romanche FZ.

4. The attributes of the internal hydraulic jump are visible in the section of three stations carried out in 2013 from Southern Entrance-1 sill to the abyss of the Southern Depression (Figure 11b). As the abyssal flow descends, its near-bottom core accelerates and the inclination of isotherms in this core is quasi-parallel to the fracture slope. The same can be seen in Figure 11a. Reaching the abyss of the Southern Depression the velocity core of the flow as a whole is somewhat slowed down and at the same time becomes thicker (Figure 11b). For example, the core thickness on the sill over isotach 18 cm/s (which delineates on the sill the core of the flow with quasi-constant velocity) was 300 m, on the slope it was 250 m, and in the deep part of the Southern Depression it was 470 m. The elevation of the isotherms from the depth in the layer $\theta > 0.8$ °C is consistent with this thickening (Figure 11b). The slowdown and thickening of the flow correspond to the shock discharge (dissipation) of the kinetic energy in the zone of hydraulic jump (Pratt & Whitehead, 2007). It is possible that station 2511 in the Southern Depression was located directly in the jump zone with very active vertical turbulent mixing, as indicated by the presence of several temperature inversions in the layer from the bottom to about 4,400 m (Figure 11b).

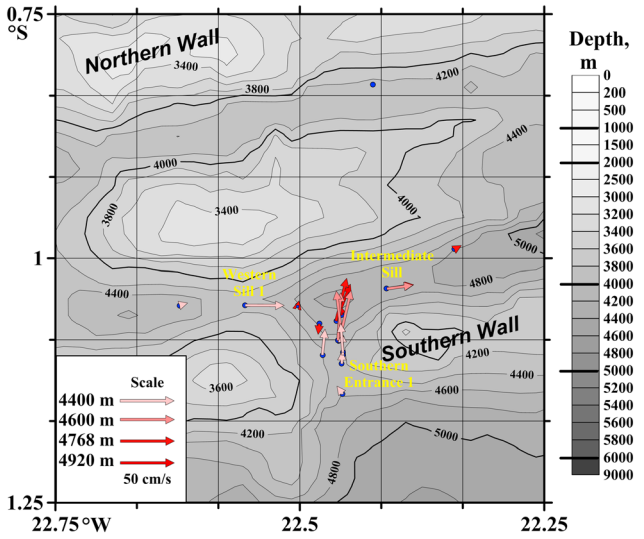

Figure 10. Velocity vectors of the abyssal flow at the entrance to the Romanche FZ based on the data of LADCP measurements at stations (blue dots) in 2011–2014. The vectors are shown at the depths approximately corresponding to the maximum velocity. Velocity vector at the station in the Northern Valley is not shown because the maximal depth at this station is less than 4,400 m. LADCP = lowered acoustic Doppler current profiler; FZ = fracture zone.

The similarity of the flow dynamics resulting from the identical spatial variability of the temperature profiles in each of the surveys (see part 4.1) suggests that the hydraulically controlled nature of the overflow through Southern Entrance-1 and Western Sill-1 existed during all of surveys. A good correspondence of the spatial distribution of velocity in the abyssal flow in Figure 10 with the distribution characterizing a hydraulically controlled overflow with the formation of an internal hydraulic jump indicates that intersurvey variability of the velocity field, as in the case of temperature, did not introduce qualitative distortions into this pattern of the flow.

One more feature of the current's field in the spillway area in Figure 10 is the existence of several locations in the Southern Depression with low velocities and even reverse (southward) currents. The explanation of their existence, given the presence of a flow that descends from the sills during each of the survey, is that these stations did not fall into the narrow jet of this flow. The presence of jet structure in the Southern Depression can also be shown by taking into account the transport balance along the flow descending from the sill. An increase in the flow velocity when it descended requires, by virtue of the condition of the transport conservation, a reduction in the area of its cross section. Based on this balance the hypothetical flow widths descending from the Southern Entrance-1 sill were estimated using the measurement data in 2013 (Figure 11b). The estimates were made assuming the horizontal homogeneity of the velocity field in the flow separately for the triangular and rectangular cross sections of the flow. The width of the passage at the sill along the bifurcation depth is 7.1 km. In the case of a triangular cross section the width of the flow on the slope was about 7.1 km at the isobath of 4,400 m (zero isotach immediately above the velocity core of the flow) and about 2.7 km at the 4,150-m isobath in the deep part of the Southern Depression; the flow widths for a rectangular section were 2.1 and 1.0 km, respectively. For comparison, the width of the Southern Depression at the 4,400- and 4,150-m isobaths on the basis of our measurements of bottom relief (Figure 2a) was 8–11 km. The above estimates indicate that abyssal flows descending from the sills in the Southern Depression form narrow jets in it, the horizontal transverse dimension of which may be substantially smaller than the size of this basin.

The lower (compared to the Southern Depression) velocities of the abyssal flow (up to 28 cm/s at station 2538, Figure 9) fixed at its ascent to the Intermediate Sill may be due to several reasons. These are the temporal variability of the intensity of this flow (at least, the transverse inhomogeneity of the velocity field) and the decrease in the kinetic energy of the flow as it rises from the depth of the Southern Depression. Since the measurements in the Intermediate Sill and Southern Depression were performed in different years, it is impossible to single out a specific reason. The overestimated transport compared with the estimated transport sum of the cross sections of Western Sill-1 and Southern Entrance-1 (see section 6) and small velocities (3–8 cm/s) at station 2467 at the northern slope of the Southern Valley (Figure 10) is consistent (although not confirming) with the idea of the jet flow at the Intermediate Sill and downstream part of the Romanche FZ. The jet structure of the flow even further downstream is unambiguously revealed by the result of the LADCP measurements of currents in the section carried out in 2011 at 22°10.5′W (Figure 2b). The total transport of the abyssal flow turned out to be negative (i.e., westward, Tarakanov et al., 2013) that in the presence of proven flow down from the upstream sills in the 2011 measurement period means that the flows directed to the east slipped through the 3-mile grid of stations of this section. Note also the measurements at station 2483 in the Northern Valley of the fracture north of the spillway zone (Figure 2b). Here the northeasterly bottom velocities of 3–5 cm/s were recorded. Small values of this velocity agree with the indirect indications mentioned in the previous sections, which indicate the absence of an intense abyssal flow in this valley.

To estimate the vertical velocities in the flow down the sills, we note that the average inclination of the bottom slope at Southern Entrance-1 is one tenth. Thus, considering that the velocities measured at the stations

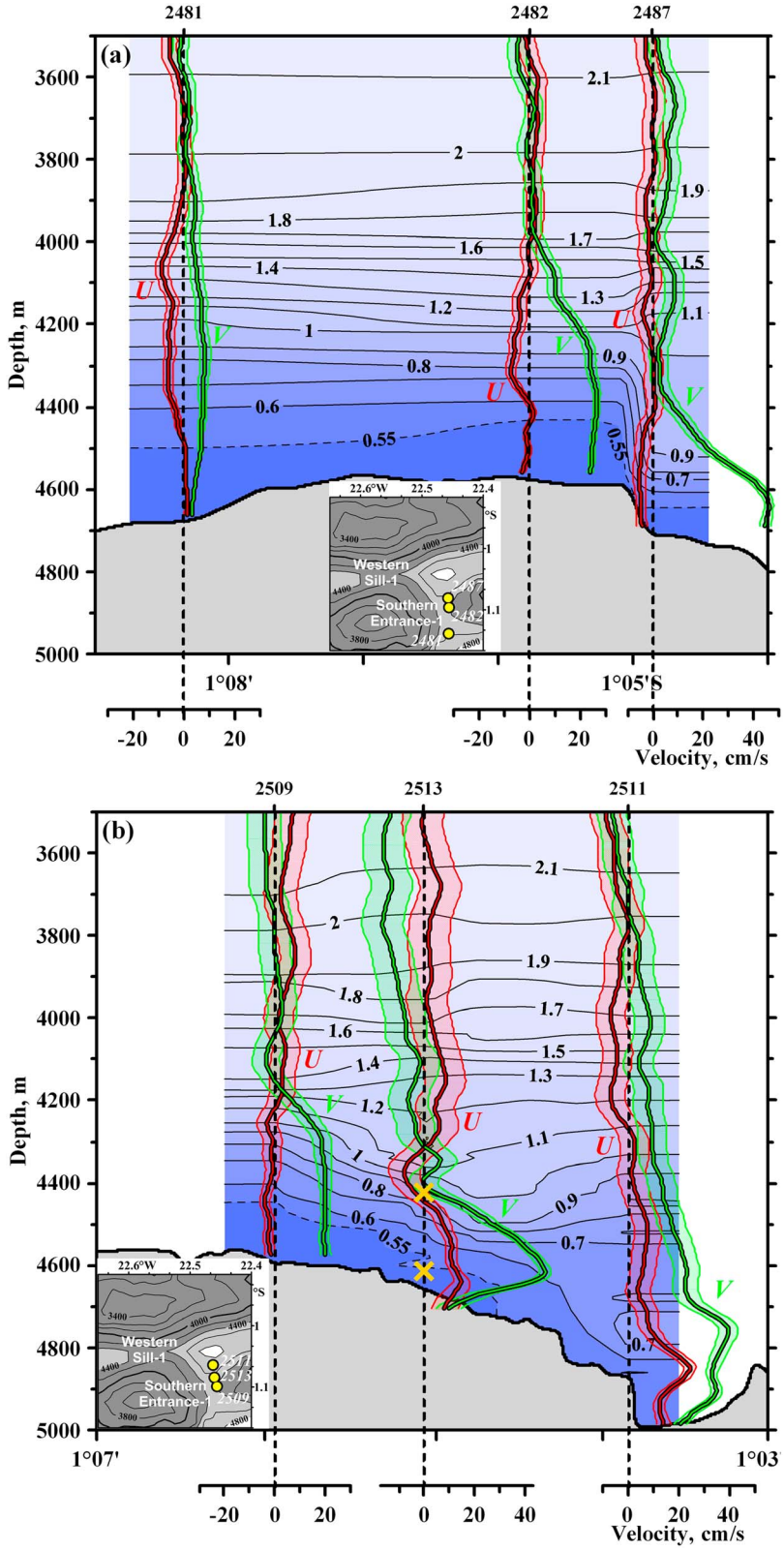

Figure 11. Distribution of potential temperature (°C) and profiles of the zonal (*U*) and meridional (*V*) current components and errors in the bottom layer over the meridional section across Southern Entrance-1 in 2012 (a), and the section from the sill of Southern Entrance-1 to the abyss of the Southern Depression in 2013. A scheme of the stations over the section is shown in the inset. Yellow crosses in Figure 11b indicate the levels of two Aquadopp current meters at 4,421 and 4,611 m.

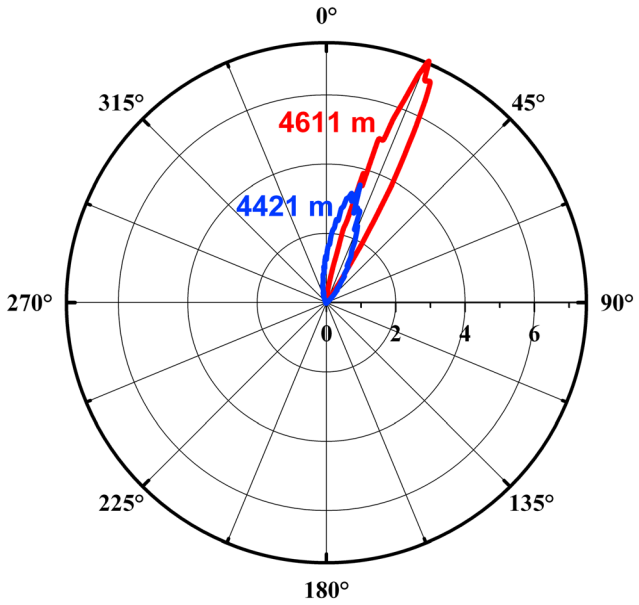

Figure 12. Distribution of the intensity of currents by directions (percent per 1° angle) over a period of 6 months based on the data of two moored current meters located at 4,421 (blue line) and 4611 m (red line).

along the bottom flow were 25–40 cm/s, the average vertical component can be estimated as 3–4 cm/s. The average inclination of the bottom of the Southern Valley of the fracture after the flow passes Western Sill-1 is 1/15. Assuming that the flow velocity does not decrease below the values measured at the sill (35 cm/s), the average vertical component can be estimated here as not less than 2.3 cm/s.

5. Mooring Observations

Moored measurements of velocities and temperature allow us to get direct estimates of temporal variability of current and temperature at the point of mooring deployment. First of all we shall analyze the average and statistical characteristics of the currents and temperature time series measured on the buoy.

5.1. Mean and Statistical Parameters

The distribution of the intensity of currents with respect to directions on the basis of the data of two current meters at the mooring station is shown in Figure 12. This diagram is similar to the transport rose from Morozov et al. (2013) in the Kane Gap. We plotted this diagram for each of the current meters. In each of the 360 one-degree sectors, the velocities, whose directions fall into this sector, were summed and then normalized by the total sum of velocities in all 360 sectors. The direction of the mean flow at the depths of the lower and upper current meters was 23° and 13°, respectively. We estimate that 95% of the measured directions appear within the range of 11–32° at the lower meter and 336–45° at the upper meter. The rotation of the mean flow direction of currents from 23° at the lower to 13° at the upper instrument is obviously caused by the influence of the bottom topography (Figure 12).

Table 2 shows the statistical characteristics of the time series of velocity component in the mean flow direction at the upper and lower current meters of the mooring and of the highest and lowest thermistors. Figure 13a, representing the time dependence of the daily average values of the mean flow velocity component, and the data in Table 2 show that the currents measured by the lower current meter are characterized by quasi-permanent high velocities (~40 cm/s) with fluctuations that are almost 1 order of magnitude smaller than the average velocity values. These values are in a good agreement with the LADCP-measured velocities (40–45 cm/s) of the same direction at three stations (2487 in 2011, 2513 in 2012, and 2537 in 2014) near the mooring point where the existence of the near-bottom jet was shown in section 4.2 of this paper using the example of the section in 2013 along the flow descending from Southern Entrance-1. This correspondence between LADCP and mooring measurements shows that the near-bottom jet in the Southern Depression is quasi-permanent. The average velocity at the level of the upper current meter is about 20 cm/s; the amplitudes of fluctuations are of the same order of magnitude as the average velocity (Figures 13a and Table 2). The vertical velocities at the deep spillway are extremely high for the open ocean (Figure 13b and Table 2). The average measured vertical velocities of the descending flow at the lower and upper current meters were 6.6 and 4.9 cm/s,

Table 2
Statistical Characteristics of the Mooring Temperature and Velocity: Vertical Component and the Component in the General Direction of the Flow ($V_{\text{mean flow}}$)

	Upper ADCMeter		Lower ADCMeter		Upper thermistor,	Lower thermistor,
	$V_{\text{mean flow}}$ (cm/s)	W (cm/s)	$V_{\text{mean flow}}$ (cm/s)	W (cm/s)	θ, (°C)	θ, (°C)
Mean	19.2	−4.9	40.7	−6.6	0.781	0.527
RMS	13.4	4.1	7.5	2.1	0.078	0.015
Maximum	56.1	10.3	66.2	2.4	1.173	0.756
Minimum	−13.2	−21.3	5.0	−15.2	0.534	0.479

Note. ADCMeter = acoustic Doppler current meter; RMS = root-mean square.

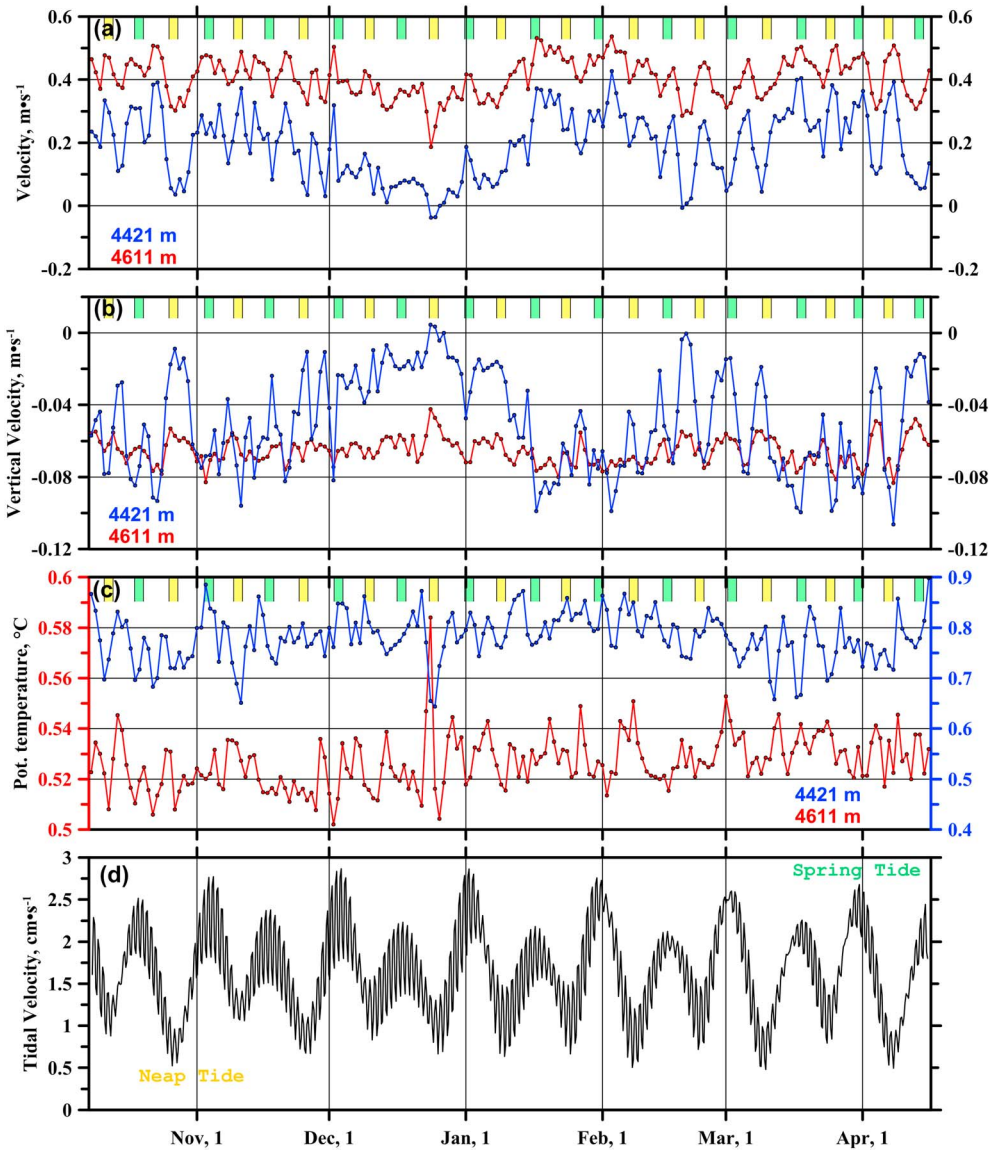

Figure 13. Daily mean current velocity component in the mean flow direction at the upper (blue line) and lower (red line) Aquadopp current meters (a), vertical velocity components (b), potential temperature at the upper and lowest temperature sensors (c), and total barotropic tide on the basis of the TPXO 7.2 (d); positive values in Figure 13b correspond to the upward direction. Yellow (green) marks at the upper axes correspond to the neap (spring) tide.

respectively; the highest instantaneous values were 15.2 and 21.3 cm/s, respectively. These mean measured velocities agree with the estimates obtained from the LADCP measurements but are slightly larger. This fact is related to the larger local bottom slope (1/6) at the location of the mooring, which was estimated from the ratio of the vertical and horizontal velocity components at the lower meter. As for the statistical characteristics of temperature (Table 2) we note that the potential temperatures near the bottom at the CTD stations at the sills of Southern Entrance-1 and Western Sill-1 (Figure 4) fall within the limits of the root-mean-square (RMS) from the average value at the lower thermistor (0.527 ± 0.015 °C) or they are slightly (by 0.003 °C) less than the lower limit due to the upstream location of these stations relative to the mooring. The smallest instantaneous value of the potential temperature near the bottom at the mooring was 0.473 °C. Thus, even colder water than that measured during CTD casts may sporadically flow into the Romanche FZ in the spillway region. Lowest and highest temperatures are conditioned by intense turbulent overturning due to the shear instability observed at the mooring location (van Haren et al., 2014).

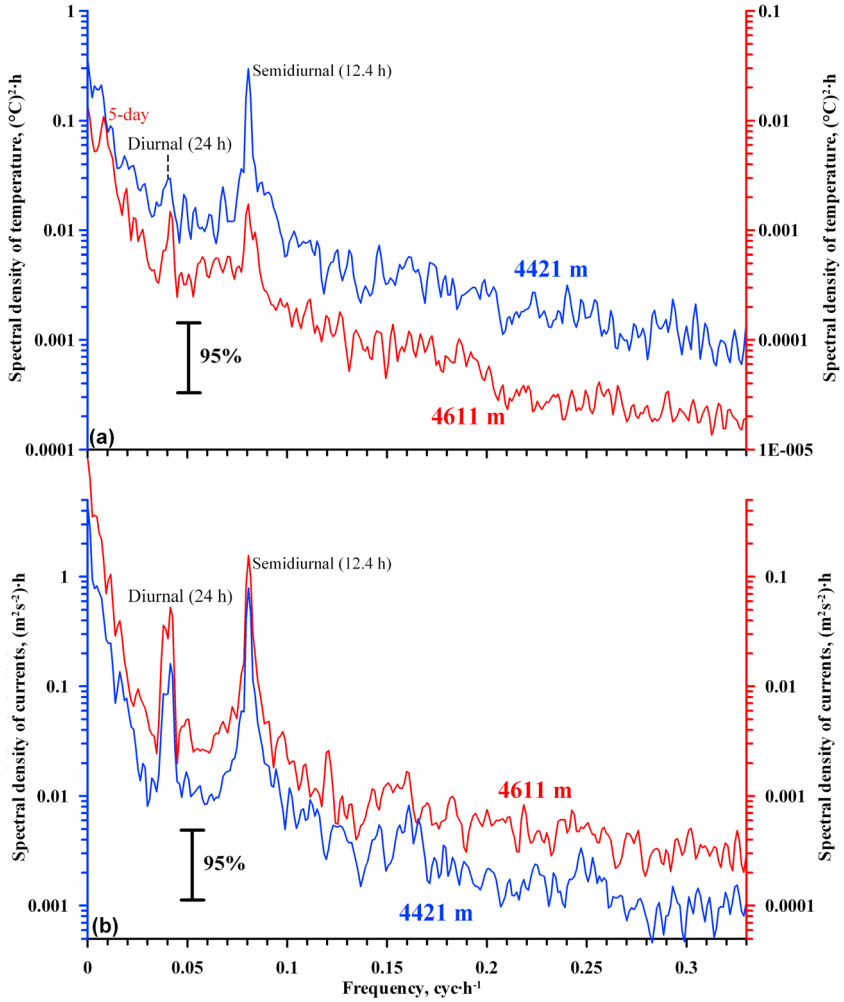

Figure 14. Spectra of potential temperature (a) and components of velocities in the mean flow direction of currents (b) at the upper (blue line) and lower (red line) thermistors.

5.2. Tidal and Temporal Variability of Temperature and Currents

Graphs of horizontal velocities in Figure 13a show high correlation at subinertial frequencies over the vertical distance between the instruments. It is obvious that there is a long-term oscillation, which we estimated as 90 days over the 189 days of velocity measurements, but the time series is too short to get a statistical reliable estimate. Both current meters recorded a minimum flow on the last days of 2013 and a maximum in the beginning of February 2014. The vertical velocities (Figure 13b) are in the negative correlation with the horizontal velocities since the velocity vector is directed along the sloping bottom. The mentioned near-90-day period is not visible in the temperature time series (Figure 13c).

All graphs of the horizontal and vertical velocity components and the graph of the lower temperature sensor (9 m above the bottom) in Figure 13 show well-correlated oscillations with a period of the order of several days (hereinafter, low-frequency oscillations) during the entire observation period. An increase in the horizontal velocities corresponds to an increase in the vertical downward velocities and a decrease in the temperature. The spectral analysis of the temperature distribution at the lower thermistor shows approximately a 5-day maximum of the spectral density (albeit statistically insignificant, Figure 14a). The temperature distribution at the upper thermistor demonstrates the segments with the positive correlation with the temperature at the lower thermistor (e.g., October 2013) and with the negative correlation (e.g., December 2013, Figure 13a). Spectral analysis of temperature distributions at the upper thermistor (Figure 14a) and velocities at both current meters (Figure 14b) does not reveal significant local maxima of the spectral density at low frequencies. A significant increase in the spectral density toward the lower

frequencies is observed in these spectra. We note that the 189-day interval of observations does not allow us to sufficiently resolve this part of the spectrum with respect to frequencies and to unambiguously separate the closely spaced maxima of the spectral density. The dominant periodicities in the current and temperature in the higher-frequency part of the spectra are diurnal (near 24 hr) and semidiurnal (12.4 hr) tidal frequencies (Figure 14).

The statistical characteristics of temperature and velocity distributions on the mooring stated above can be commented as follows.

1. The negative correlation of temperature and horizontal velocity on the lower sensor shows that, as the velocity of the overflow increases, the depth from which the uplift is made from the fracture south of the Romanche FZ to the sill of Southern Entrance-1 also increases. Thus, as was assumed in section 4.2, the Southern Wall in the mean overflow conditions blocks the uplift of the deepest cold layers from the south.
2. Since the temperature fluctuations of the upper sensor many times exceed the oscillations at the lower, it is the upper sensor that qualitatively reflects the oscillations of the average density stratification of the bottom layer at the mooring point. A temperature increase at the upper sensor (i.e., an increase in the temperature difference between the upper and lower thermistor) corresponds to an increase in stratification; a fall of temperature is a decrease in stratification. The variability of density stratification at the mooring point may be due to the temporal variability of the stratification of the overflowing flow itself or to the establishment of the stratification typical for the Southern Depression in the slow-motion phase at the mooring point due to the shift of these weakly stratified waters toward the sill or even the termination of the hydraulic regime control overflow. The temperature increase/decrease at the upper sensor in this phase depends on its location relative to the depths at which the isotherms rise in the direction of the jump. As can be seen from Figure 11b, the level of the upper thermistor in the section of 2013 along the descending flow was exactly in this range in its lower part. The shift of the temperature profile from the Southern Depression to the mooring point would decrease the temperature of the upper thermistor. The most striking manifestation of this situation is the period in the end of December 2013 when the minimum daily and instantaneous velocities were recorded as well as the maximum temperature at the lower level, and the maximum daily and instantaneous negative velocities and one of the lowest temperatures at the upper level were found (Figure 13 and Table 2). If the depth range corresponding to the rise of the isotherms in the direction of the jump is above the level of the upper thermistor, then shifting the more weakly stratified waters from the Southern Depression toward the sill or termination of the hydraulic control overflow would cause the temperature increase at the upper thermistor. This situation of positive correlation of the lower and upper thermistors was observed, for example, in the first half of October 2013 (Figure 13).
3. Clément et al. (2017) showed the determinative influence of spring-neap modulation (14-day cycle) on turbulent mixing and overflow regime in the canyon narrows/sills in the South Atlantic Ridge fractures in the Brazil basin. To illustrate the role of this modulation in the Romanche FZ, we show in Figure 13d the distribution of the absolute values of the total tidal velocity on the basis of TPXO 7.2. Comparison of this distribution with the remaining curves in Figure 13 shows that the episode of the end of December 2013 described above with an extreme slow motion of the flow corresponds to a neap tide. Such a correspondence indicates the influence of spring-neap modulation on the overflow regime in the spillway of the Romanche FZ, although it is not detected by the spectral analysis. At the same time, there is no correlation of quick/slow motion episodes with the spring/neap period in general.

The time series of velocities were band filtered to find the dominating directions (Tukey filter). A bandwidth (without edge cutting) of 1/11.9–1/12.9 per hour was chosen for the semidiurnal tide. The distributions of direction of the semidiurnal range of currents at the upper and lower meters are shown in Figure 15. The main directions of the semidiurnal tidal currents at the lower and upper current meters do not coincide. At the lower current meter, they fluctuate around opposing directions 45° and 225°. The corresponding directions at the upper instrument are 22° and 202°. Directions of fluctuations of the diurnal tide (cutoff at 1/23.2 to 1/24.8) are almost the same as the directions of the semidiurnal tidal fluctuations at the depths of both current meters. The fluctuations of directions in the low-frequency range also fall into the tidal direction range. Figure 15 shows the distribution of intensities of the total barotropic tide over directions

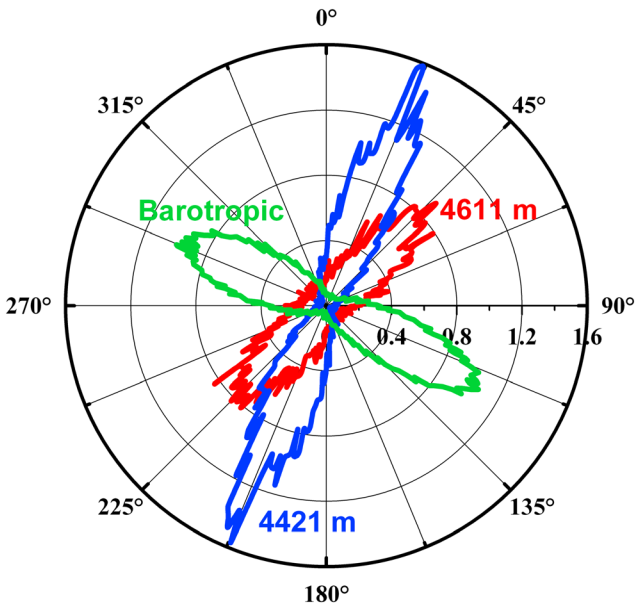

Figure 15. Distribution of the intensity of semidiurnal tidal currents by directions (percent per 1° angle) over a period of 6 months based on the data of two moored current meters located at 4,421 (blue line) and 4,611 m (red contour), and full barotropic tide (TPXO 7.2) (green).

according to the TPXO 7.2 model, also averaged over 6 months. The main direction of the ellipse of the total barotropic tide is almost normal (115–295°) to the direction of the tide at the upper current meter. Note that the fluctuations of the model barotropic tide are related to the entire water column.

The intensity of fluctuations in different frequency bands is well illustrated in Figure 16, where the cumulative (from zero frequency) distributions of the specific kinetic energy of fluctuations for two current meters are shown. The total specific energy of the oscillations at the upper and lower current meters is estimated at 89 and 28 cm^2/s^2, which is equivalent to the RMS of current velocities of 13.4 and 7.5 cm/s (Table 2), respectively. About 70% of the total oscillation energy both at the lower and upper meters is related to the low-frequency part of the spectrum, 38–45% of which is the energy of oscillations with periods from 2 to 12 days. The high-low-frequency cutoffs at 1/11 and 1/14 cph were used for the semidiurnal tide (central frequency of 1/12.4 cph, Lozovatsky et al., 2003), and at 1/22 and 1/28 cph for the diurnal tide. Thus, about 10–15% and 4–5% of energy is concentrated at the semidiurnal and diurnal tidal frequencies, respectively. We note that the velocities corresponding to tidal oscillations are many times smaller than the mean values of the flow velocities (Table 2). This means that the temporal variability at these periods during each survey (lasting about 1 day) corresponding to the average statistical conditions was small compared to the average flow characteristics.

The energies and velocities corresponding to all of the mentioned frequency ranges are shown in Figure 16. For comparison, Figure 16 also shows the energy level of the barotropic tide, which is approximately 30 times smaller than the total energy of oscillations at the lower current meter and 100 times smaller compared with the upper one. Thus, we can conclude that not the barotropic tide energy but the available potential energy of the deep thermocline, which transforms to the kinetic energy in the zone of the overflow, seems to be the main source of the fluctuation energy at the location of the mooring in the Romanche FZ. At the same time, the energy transfer to predominantly low frequency fluctuations is observed. The origin of these low frequencies, with the exception of spring-neap period, cannot be established from the available data set. For example, these oscillations can be seiches or fluctuations in the available potential energy of a deep thermocline. Note that recently (Clément et al., 2017) fluctuations of the kinetic energy somewhat smaller in magnitude but many times exceeding the energy of the barotropic tide were recorded by moorings in the canyon narrows/sills in the fracture at 21°S in the Brazil basin.

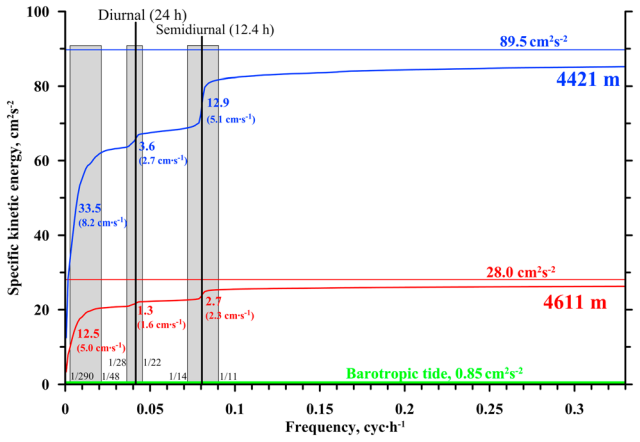

Figure 16. Cumulative specific kinetic energy of oscillation as a function of frequency at 4,421 (blue curve) and 4,611 m (red curve). The levels of the total energy of the fluctuations and the energy of the barotropic tide are shown. Energies and RMS velocities corresponding to the frequency bands identified by the gray rectangles are also given. RMS = root-mean-square.

6. Transport of Abyssal Waters in the Deep Spillway Region

Calculations of the abyssal flow transport were carried out according to the formula:

$$Q = \sum_{i=1,n} \left(\sum_{z_{1_j}}^{z_{2j}} U_i(z) w_i(z) \Delta z \right) \pm \sqrt{\sum_{i=1,n} (\delta Q_i)^2}, \quad (2)$$

where n is the total number of stations in the cross section across the passage, $U_i(z)$ is the component of the measured velocity transverse to the cross section of the passage, $w_i(z)$ is the width of the cross-section segment at depth z corresponding to the ith station (the width of the passage if only one station was made), and δQ_i is the transport error calculated on the basis of the formal error of the current velocity $\delta U_i(z)$ evaluated in turn by the LADCP software package:

Table 3
AABW Transports Based on the Data of LADCP Measurements and Bottom Potential Temperature in Different Parts of the Cataract in the Romanche FZ (see Figure 2b)

Year	Place of measurements	Transport in the layer $\theta < 1.2$ °C (Sv)	Transport in the layer $1.2 < \theta < 1.7$ °C (Sv)	Bottom potential temperature (°C)
2011	Southern Entrance-1 (station 2472)	0.08 ± 0.05	0.00 ± 0.11	0.508
2012	Southern Entrance-1 (station 2482)	0.28 ± 0.02	0.11 ± 0.05	0.513
	Western Sill-1 (station 2480)	0.07 ± 0.01	0.00 ± 0.03	0.534
	Total	0.35 ± 0.02	0.11 ± 0.06	
2013	Southern Entrance-1 (stations 2509, 2510)	0.19 ± 0.02	0.04 ± 0.04	0.506
	Western Sill-1 (station 2515)	0.10 ± 0.04	0.01 ± 0.07	0.525
	Total	0.29 ± 0.04	0.05 ± 0.08	
2014	Intermediate Sill in the Southern Valley of Romanche FZ (station 2538)	0.44 ± 0.08	0.14 ± 0.12	0.613
2011	Southern Valley of Romanche FZ (station 2467)	0.23 ± 0.19	0.22 ± 0.18	0.660

Note. AABW = Antarctic Bottom Water; LADCP = lowered acoustic Doppler current profiler; FZ = fracture zone.

$$\delta Q_i = \sqrt{\sum_{z_{1_i}}^{z_{2_i}} (\delta U_i(z))^2 w_i(z) \Delta z \sum_{z_{1_i}}^{z_{2_i}} w_i(z) \Delta z}. \quad (3)$$

Table 3 shows the estimates of abyssal flow transports through several sections in the Romanche FZ based on the LADCP measurements in 2011 (Tarakanov et al., 2013) and in 2012–2014. It is clear from the above formulas that we assumed that the flow structure is homogeneous in the horizontal transverse-to-the-flow direction, that is, that the flow velocity is constant over the cross section. We excluded from the calculations all the stations inside the Southern Depression due to the revealed horizontal inhomogeneity of the field of currents there as well as at station 2481 located south of Southern Entrance-1 sill already on the northern slope of the adjacent fracture for which the bottom relief measurements in cross section were not performed.

The most reliable estimates of the transport across all individual cross sections in the layer $\theta < 1.2$ °C are those at the sill of Southern Entrance-1 in 2012 and 2013. This statement is based on the following.

1. A section of two stations in 2013 across the gap of Southern Entrance-1 at the sill was made to test the horizontal homogeneity of the flow. These measurements showed that the maximal horizontal velocity below the bifurcation depth varies very little across the gap (from 20 to 25 cm/s, Figures 8a and 8b).
2. As shown in section 4.2, the transport estimates and the measured velocities are in good agreement with the predicted transport and the corresponding gravity wave speed for this sill, thereby confirming that this cross section is close to the hydraulically control point. Since the hydrographic conditions between surveys are similar (see section 4.1), they are close to the mean conditions, and oscillations at tidal periods in these conditions are small (see section 5.2), the close values of the velocities (20 to 25 cm/s) and transports measured in 2012 and 2013 are quite natural. Based on the same considerations the flow in the section south of Southern Entrance-1 sill in 2011 seems to be underestimated apparently due to the horizontal inhomogeneity of the flow in the wider cross section before this sill, where only one station was made in 2011.

Although we cannot assess the horizontal homogeneity of the flow at Western Sill-1 in 2012 and west of it in 2013, the reliability of the transports in the layer $\theta < 1.2$ °C is maintained by their correspondence to the predicted values that are many times less than those through Southern Entrance-1. The sum of transports at Southern Entrance-1 and Western Sill-1 gives estimates of the total transport in this layer from two velocity profiles in 2012 and three in 2013. On the basis of these considerations we conclude that these LADCP measurements approximate quite well the average transport values in the spillway in the layer $\theta < 1.20$ °C (Table 3). This transport is 0.29–0.35 Sv, which is about 50–60% of the total eastward directed transport of AABW (0.6 Sv) estimated in Mercier and Speer (1998) and Morozov et al. (2010) in the middle part of the fracture (16°W). Two more sections over Intermediate Sill in 2014 and in 2011, the east of this sill (Table 3), give a complete estimate of the total transport on the basis of only one profile while horizontal flow inhomogeneity may be significant.

Table 3 also shows the estimates of the transport in the water layer $1.20 < \theta < 1.70$ °C. A limitation from above is due to the result of the analysis of the bottom topography along the Romanche FZ (Tarakanov et al., 2013). This analysis showed that downstream of the study area both in the Northern and in the Southern Walls of the fracture before the watershed line between the West and East Atlantic there are several passages (at 18°–19°30′W) reaching the depth of the isotherm $\theta = 1.70$ °C (~4,000 m) through which the water exchange with the surrounding basins can occur. Additional water exchange in the water layer $1.20 < \theta < 1.70$ °C between the downstream part, the Romanche FZ and the West Atlantic, seems substantially more limited. The bottom water in this temperature range, in addition to Southern Entrance-1 and Western Sill-1, can pass through the Northern Valley of the fracture. Water exchange through the passages at 18°–19°30′W can occur only in the case of a significant underestimation of the depth of these passages in the database (Smith & Sandwell, 1997). As can be seen from Figures 8 and 11b, oppositely directed currents are observed over the 1.20 °C isotherm even above the sill of Southern Entrance-1, that is, horizontal inhomogeneity of the flows exists in this layer. This fact makes us consider that the estimates of transport in this layer are unreliable. The unreliable values of these transports also follow from the estimates of transport accuracy in this layer, which is equal and even greater than the transport estimates (Table 3). In spite of this, we note that the total water transport in the layer $1.20 < \theta < 1.70$ °C is roughly consistent with the above mentioned topographic limitation for this layer and total AABW transport in the middle part of the fracture (16°W). On the one hand, it is positive, and, on the other, its sum with the transport in the layer $\theta < 1.20$ °C does not exceed the total AABW transport.

7. Summary

Structure of the deep spillway was studied on the basis of CTD, LADCP, and mooring measurements in 2011–2014 in the western part of the Romanche FZ (22°27′–22°32′W). The spillway consists of two flows and exists in the layer $\theta < 1.20$ °C (deeper than 4,150 m). The first flow enters the fracture from the south through the gap in the Southern Wall with a sill depth of about 4,570 m (Southern Entrance-1, 1°05′S, 22°27′W). The second flow is directed to the east along the narrow channel of the fracture with a sill depth of about 4,430 m (Western Sill-1, 1°03′S, 22°34′W). The characteristic depths over the surrounding ridges are much smaller than 4,100 m. Both flows descend to the same local Southern Depression with a depth of 5,000 m, merge, and rise to the Intermediate Sill (4,870 m) of the fracture east of the depression.

All of four surveys 2011–2014 with CTD/LADCP measurements were characterized by the same rearrangement of vertical temperature profiles between the upstream sills and the interior of the Southern Depression, that is, the spatial variability of the temperature field between these regions during the measurement periods is much greater than the temporal (intersurvey) variability of this field. This rearrangement means the presence of a hydrostatic pressure difference directed from the sills into the Southern Depression increasing with depth with nearly the same values in different years. This pressure difference sets the abyssal flow in motion with nearly the same (both qualitatively and quantitatively) dynamics of currents in each survey measurements.

The values of CTD-measured temperature near the bottom increase as a whole from the Western Sill-1 and Southern Entrance-1 into the Southern Depression, where the temperature increases most strongly, and then to the east through the Intermediate Sill to the deep part of the Romanche FZ. This increase ranges from 0.506–0.534 °C at the upstream sills to 0.612 °C at the Intermediate Sill and to 0.648 °C in the deep part. The velocities of the abyssal flow were measured as 5–10 cm/s in front of Southern Entrance-1 and Western Sill-1, as 20–25 cm/s at Southern Entrance-1, and as 35 cm/s on Western Sill-1. The maximum velocity at the stations (up to 48 cm/s) was measured on the slope of the Romanche FZ at Southern Entrance-1. Lower velocities up to 28 cm/s were found at the Intermediate Sill. Such velocity and temperature fields correspond a hydraulically controlled overflow across Southern Entrance-1 and Western Sill-1, when the flow is accelerated in the subcritical regime (Froude number $Fr < 1$) before the control point (sill or narrow), reaches critical regime ($Fr = 1$) at this point, and transfers to the supercritical ($Fr > 1$) after its passage with a return to the subcritical regime downstream in the form of a hydraulic jump where maximal turbulent mixing takes place. Several more indirect evidences of hydraulic control overflow across the upstream sills exist.

One more feature of the current's field in the spillway is a formation of narrow jets of the flow descending from the sills into the Southern Depression and farther to the east. The horizontal transverse dimension of

these jets may be substantially smaller than the size of this basin. This feature is confirmed by the estimates of the hypothetical flow width based on the transport balance along the flow descending from Southern Entrance-1, the existence of reversal (southward) velocities in the Southern Depression in the presence of proven northward spill from Southern Entrance-1 at the moment of measurements, and some other evidences.

The potential temperature measured by the lowest thermistor of the mooring (at 9 m from the bottom) deployed in the flow descending from the sill of Southern Entrance-1 was 0.527 ± 0.015 °C (mean ± RMS). The minimum potential temperature measured by the mooring was 0.479 °C. The mean horizontal velocities based on the data of the mooring were approximately 40 cm/s; the maximum recorded horizontal velocities were 65 cm/s. The average vertical downward velocity components near the bottom based on the mooring measurements were 6.6 cm/s, and the maximum velocities were 15 cm/s. The average value is in a good agreement with the indirect estimation based on the LADCP measurements. The bottom inclination at the mooring location based on the ratio of the vertical and horizontal velocity components is one sixth. The mean slope of the bottom along this flow in the spillway based on the echo-sounder measurements is estimated at one tenth.

Comparison of CTD and mooring measurements shows that the bottom temperature near the sills is in the range of mean ± RMS values evaluated by the lowest thermistor of the mooring. Besides, the average values of the velocities measured at the lowest ADCMeters are in a good agreement with the velocities measured by LADCP at the same level near the mooring point where bottom jet exists. These results indicate that hydraulic control overflow across Southern Entrance-1 and Western Sill-1, and jet formation in the Southern Depression and farther east are the quasi-permanent feature of the velocity's field in the spillway in the Romanche FZ.

Analysis of the 189-day time series of velocity measurements on the mooring showed a very high level of fluctuation energy for the open ocean. The total specific energy of fluctuations is estimated at the mooring location as 28 cm^2/s^2 at a distance of 200 m from the bottom and as 89 cm^2/s^2 near the bottom, which is equivalent to the RMS of the velocities of 13.4 and 7.5 cm/s, respectively. Approximately 10–15% and 4–5% of this energy is related to the semidiurnal (~12.4 hr) and diurnal (~24 hr) frequency ranges, respectively. About 70% of the total fluctuation energy corresponds to the low frequencies (the periods exceeding 2 days), 40% of which corresponds to the periods of 2–12 days. These energies exceed many times the energy of the barotropic tide, which is estimated at 0.85 cm^2/s^2 (TPXO7.2 model). Thus, the only energy source of the fluctuations measured by the mooring is the available potential energy of the deep thermocline of the West Atlantic transforming to the kinetic energy of the deep spillway. Note that the origin of the low frequencies at the mooring location, with the exception of spring-neap period, cannot be established from the available data set. For example, these can be seiche oscillations or fluctuations in the available potential energy of the deep thermocline. The dominating periodicities in the temperature in the higher-frequency range of the spectra are diurnal (near 24 hr) and semidiurnal (near 12.4 hr) tidal frequencies.

The transport of bottom water below the θ = 1.2 °C isotherm (i.e., in the layer of the deep spillway) based on the LADCP measurements through Southern Entrance-1 and Western Sill-1 is estimated at 0.19–0.28 and 0.07–0.10 Sv, respectively. These values are in a good agreement with the predicted values 0.24 and 0.06 Sv, respectively, calculated using 1.5 layer model of hydraulically controlled flow between two basins through a channel with a rectangular cross section (Whitehead et al., 1974). Several more indirect evidences of a reliability of the LADCP based transport estimates exist. The sum transport through these sills is a total transport below θ = 1.2 °C estimated at 0.29–0.35 Sv. It is 50–60% of the well-known estimate of the total AABW eastward transport (0.6 Sv in the layer colder than 1.9 °C) through the Romanche FZ in its middle part. The total transport between θ = 1.2 and θ = 1.7 °C is 0.05–0.11 Sv. In spite of the unreliability of these estimates they are roughly consistent with the topography limitations for the water exchange of the Romanche FZ at and east of the spillway meridian with the surrounding basins, and the mentioned total AABW transport in the middle part of the fracture (16°W).

Acknowledgments
We thank J. Whitehead and an anonymus second reviewer for their constructive formal reviews of this paper. We thank the crew of the R/V *Akademik Sergey Vavilov* for their assistance in deployment and recovery of the mooring. Field studies were financed by the programs of the Russian Academy of Sciences and the state assignments of Russia. The analysis was supported by the Russian Science Foundation grant 16-17-10149. Data used in the analysis are available from https://doi.pangaea.de/10.1594/PANGAEA.893182 and https://doi.pangaea.de/10.1594/PANGAEA.893175.

References

Baines, P. G., & Condie, S. (1998). Observation and modelling of Antarctic downslope flows: A review. In S. S. Jacobs, & R. F. Weiss (Eds.), *Ocean, ice, and atmosphere: Interactions at the Antarctic continental margin*, *Antarctic Research Series* (Vol. 75, pp. 29–49). Washington DC: American Geophysical Union. https://doi.org/10.1029/AR075p0029

Bryden, H. L., & Nurser, A. J. G. (2003). Effect of strait mixing on ocean stratification. *Journal of Physical Oceanography*, *33*(8), 1870–1872. https://doi.org/10.1175/1520-0485(2003)033<1870:EOSMOO>2.0.CO;2

Clément, L., Thurnherr, A. M., & St Laurent, L. C. (2017). Turbulent mixing in a deep fracture zone on the Mid-Atlantic Ridge. *Journal of Physical Oceanography*, *47*(8), 1873–1896. https://doi.org/10.1175/JPO-D-16-0264.1

Demidov, A. N., Morozov, E. G., & Neiman, V. G. (2006). Structure and variability of deep waters in the Romanche fracture zone. *Doklady Earth Sciences*, *410*(1), 1136–1140. https://doi.org/10.1134/S1028334X06070300

Demidov, A. N., Morozov, E. G., & Tarakanov, R. Y. (2012). Structure and transport of bottom waters through the Chain fracture zone of the Mid-Atlantic Ridge. *Russian Meteorology and Hydrology*, *36*(8), 542–548. https://doi.org/10.3103/S1068373911080061

Egbert, G. D., & Erofeeva, S. (2002). Efficient inverse modeling of barotropic ocean tides. *Journal of Atmospheric and Oceanic Technology*, *19*(2), 183–204. https://doi.org/10.1175/1520-0426(2002)019<0183:EIMOBO>2.0.CO;2

Ferron, B., Mercier, H., Speer, K., Gargett, A., & Polzin, K. (1998). Mixing in the Romanche fracture zone. *Journal of Physical Oceanography*, *28*(10), 1929–1945. https://doi.org/10.1175/1520-0485(1998)028<1929:MITRFZ>2.0.CO;2

Foster, T. D., & Carmack, E. C. (1976). Frontal zone mixing and Antarctic bottom water formation in the southern Weddell Sea. *Deep Sea Research*, *23*(4), 301–317. https://doi.org/10.1016/0011-7471(76)90872-X

Gregg, M. C. (1989). Scaling turbulent dissipation in the thermocline. *Journal of Geophysical Research*, *94*(C7), 9686–9698. https://doi.org/10.1029/JC094iC07p09686

Hall, M. M., McCartney, M., & Whitehead, J. A. (1997). Antarctic bottom water flux in the equatorial western Atlantic. *Journal of Physical Oceanography*, *27*(9), 1903–1926. https://doi.org/10.1175/1520-0485(1997)027<1903:ABWFIT>2.0.CO;2

Heezen, B. C., Bunce, E., Hersey, J., & Tharp, M. (1964). Chain and Romanche fracture zones. *Deep Sea Research*, *11*(1), 11–33. https://doi.org/10.1016/0011-7471(64)91079-4

Heezen, B. C., Gerard, R. D., & Tharp, M. (1964). The Vema fracture zone in the equatorial Atlantic. *Journal of Geophysical Research*, *69*(4), 733–739. https://doi.org/10.1029/JZ069i004p00733

Hogg, N. G. (2001). Quantification of the deep circulation. In G. Siedler, J. Church, & J. Gould (Eds.), *Ocean circulation and climate: Observing and modelling the global ocean*, *International Geophysics Series* (Vol. 77, pp. 259–270). London: Academic Press.

Kinder, T. H., & Bryden, H. L. (1990). The aspiration of deep waters through straits. In L. J. Pratt (Ed.), *The physical oceanography of sea straits* (pp. 295–319). Netherlands: Kluwer Academic Publishers.

Lherminier, P., Mercier, H., Gourcuff, C., Alvarez, M., Bacon, S., & Kermabon, K. (2007). Transports across the 2002 Greenland-Portugal Ovide section and comparison with 1997. *Journal of Geophysical Research*, *112*, C07003. https://doi.org/10.1029/2006JC003716

Limeburner, R., Whitehead, J. A., & Cenedese, C. (2005). Variability of Antarctic bottom water flow into the North Atlantic. *Deep Sea Research, Part II*, *52*(3–4), 495–512. https://doi.org/10.1016/j.dsr2.2004.12.012

Lozovatsky, I. D., Morozov, E. G., & Fernando, H. J. S. (2003). Spatial decay of energy density of tidal internal waves. *Journal of Geophysical Research*, *108*(C6), 3201. https://doi.org/10.1029/2001JC001169

Mantyla, A. W., & Reid, J. L. (1983). Abyssal characteristics of the World Ocean waters. *Deep-Sea Research*, *30*(8), 805–833. https://doi.org/10.1016/0198-0149(83)90002-X

McCartney, M. S., Bennet, S. L., & Woodgate-Jones, M. E. (1991). Eastward flow through the Mid-Atlantic Ridge at 11° N and its influence on the abyss of the eastern basin. *Journal of Physical Oceanography*, *21*(8), 1089–1121. https://doi.org/10.1175/1520-0485(1991)021<1089:EFTTMA>2.0.CO;2

Mercier, H., & Bryden, H. (1994). Flow of Antarctic bottom water over the sill in the Romanche fracture zone. *International WOCE Newsletter*, *7*, 9–10.

Mercier, H., & Morin, P. (1997). Hydrography of the Romanche and Chain fracture zones. *Journal of Geophysical Research*, *102*(C5), 10373–10389. https://doi.org/10.1029/97JC00229

Mercier, H., & Speer, K. G. (1998). Transport of bottom water in the Romanche fracture zone and the chain fracture zone. *Journal of Physical Oceanography*, *28*(5), 779–790. https://doi.org/10.1175/1520-0485(1998)028<0779:TOBWIT>2.0.CO;2

Mercier, H., Speer, K. S., & Honnorez, J. (1994). Romanche flow pathways of bottom water through the Romanche and Chain fracture zones. *Deep-Sea Research*, *41*(10), 1457–1477. https://doi.org/10.1016/0967-0637(94)90055-8

Messias, M.-J., Andrié, C., Mémery, L., & Mercier, H. (1999). Tracing the North Atlantic deep water through the Romanche and Chain fracture zones with chlorofluoromethanes. *Deep Sea Research, Part I*, *46*(7), 1247–1278. https://doi.org/10.1016/S0967-0637(99)00005-9

Monin, A. S. (1988). *Theoretical principles of geophysical hydrodynamics*. (in Russian). Leningrad: Gidrometeoizdat.

Morozov, E. G., Demidov, A. N., Tarakanov, R. Y., & Zenk, W. (2010). In G. Weatherly (Ed.), *Abyssal channels in the Atlantic Ocean: Water structure and flows* (p. 266). Dordrecht: Springer.

Morozov, E. G., Tarakanov, R. Y., & van Haren, H. (2013). Transport of AABW through the Kane Gap, tropical NE Atlantic Ocean. *Ocean Science*, *9*(5), 825–835. https://doi.org/10.5194/os-9-825-2013

Morozov, E. G., Tarakanov, R. Y., Demidova, T. A., & Makarenko, N. I. (2017). Measurements of bottom currents in the western part of the Romanche fracture zone on cruises 37 and 38 of the R/V Akademik Sergey Vavilov. *Oceanology*, *57*(5), 751–752. https://doi.org/10.1134/S0001437017050125

Morozov, E. G., Tarakanov, R. Y., Frey, D. I., Demidova, T. A., & Makarenko, N. I. (2018). Bottom water flows in the tropical fractures of the northern Mid-Atlantic Ridge. *Journal of Oceanography*, *74*(2), 147–167. https://doi.org/10.1007/s10872-017-0445-x

Morozov, E. G., Tarakanov, R. Y., Lyapidevskii, V. Y., & Makarenko, N. I. (2012). Abyssal cataracts in the Romanche and Chain fracture zones. *Doklady Earth Sciences*, *53*(6), 655–667. https://doi.org/10.1134/S0001437013050147

Munk, W. H., & Wunsch, C. (1998). Abyssal recipes II: Energetics of tidal and wind mixing. *Deep-Sea Research*, *45*(12), 1977–2010. https://doi.org/10.1016/S0967-0637(98)00070-3

Polzin, K. L., Speer, K. G., Toole, J. M., & Schmitt, R. W. (1996). Intense mixing of Antarctic bottom water in the equatorial Atlantic Ocean. *Nature*, *380*(6569), 54–57. https://doi.org/10.1038/380054a0

Pratt, L. J., & Whitehead, J. A. (2007). *Rotating hydraulics: Nonlinear topographic effects in the ocean and atmosphere*. New York: Springer.

Schmitz, W. J. (1996). On the World Ocean circulation: Volume I, Some global features. *North Atlantic Circulation* (technical report WHOI–96–03). Woods Hole: Woods Hole Oceanographic Institution 142 p.

Smith, W. H. F., & Sandwell, D. T. (1997). Global seafloor topography from satellite altimetry and ship depth soundings. *Science*, *277*(5334), 1956–1962. https://doi.org/10.1126/science.277.5334.1956

Tarakanov, R. Y., Makarenko, N. I., & Morozov, E. G. (2013). Antarctic bottom water flow in the western part of the Romanche fracture zone based on the measurements in October of 2011. *Oceanology*, *53*(6), 655–667. https://doi.org/10.1134/S0001437013050147

Tarakanov, R. Y., Morozov, E. G., Makarenko, N. I., Frey, D. I., & Demidova, T. A. (2017). Measurements of bottom currents in fractures of the southern part of the Mid-Atlantic Ridge on Cruises 39, 40, and 41 of the R/V Akademik Sergey Vavilov. *Oceanology*, *57*(5), 753–755. https://doi.org/10.1134/S0001437017050174

van Aken, H. M. (2007). The oceanic thermohaline circulation: An introduction. In *Atmospheric and oceanographic sciences library* (Vol. 39, 304 pp.). New York: Springer-Verlag.

van Haren, H., Gostiaux, L., Morozov, E., & Tarakanov, R. (2014). Extremely long Kelvin–Helmholtz billow trains in the Romanche fracture zone. *Geophysical Research Letters*, *41*, 8445–8451. https://doi.org/10.1002/2014GL062421

Vangriesheim, A. (1980). Antarctic bottom water flow through the Vema fracture zone. *Oceanologica Acta*, *3*(2), 199–207.

Visbeck, M. (2002). Deep velocity profiling using lowered acoustic Doppler current profiler: Bottom track and inverse solution. *Journal of Atmospheric and Oceanic Technology*, *19*(5), 794–807. https://doi.org/10.1175/1520-0426(2002)019<0794:DVPULA>2.0.CO;27

Whitehead, J. A. (1989). Giant ocean cataracts. *Scientific American*, *260*(2), 50–57. https://doi.org/10.1038/scientificamerican0289-50

Whitehead, J. A. (1998). Topographic control of oceanic flows in deep passages and straits. *Reviews of Geophysics*, *36*(3), 423–440. https://doi.org/10.1029/98RG01014

Whitehead, J. A., Leetma, A., & Knox, R. A. (1974). Rotating hydraulics of strait and sill flows. *Geophysical Fluid Dynamics*, *6*(2), 101–125. https://doi.org/10.1080/03091927409365790

Whitehead, J. A., & Worthington, L. V. (1982). The flux and mixing rates of Antarctic bottom water within the North Atlantic. *Journal of Geophysical Research*, *87*(C10), 7903–7924. https://doi.org/10.1029/jc087ic10p07903

Wüst, G. (1936). Schichtung und Zirkulation des Atlantischen Ozeans. In A. Defant (Ed.), *Wissenschaftliche Ergebnisse, Deutsche Atlantische Expedition auf dem Forschungs—und Vermessungsschiff "Meteor"* 1925–1927 (Vol. 6(1), 410 pp.). Berlin: Walter de Gruyter & Co.